S. Ricci, F. Toffol, A. De Gaspari, L. Marchetti, F. Fonte, L. Riccobene, P. Mantegazza, J. Berg, E. Livne, K. Morgansen
Wind Tunnel System for Active Flutter Suppression Research: Overview and Insights
AIAA Journal, published online 31/10/2022
doi:10.2514/1.J061985

The Development of a Wind Tunnel System for Active Flutter Suppression Research: Overview and Insights

S. Ricci[1], F. Toffol,[2] A. De Gaspari,[3] L. Marchetti[4], F. Fonte,[5] L. Riccobene,[6] and P. Mantegazza[7]
Politecnico di Milano, via La Masa 34, 20156 Milano, Italy

J. Berg[8], E. Livne[9] and K. Morgansen[10]
University of Washington, Seattle, WA 98195 – 2400

Abstract

The paper describes the development of a new state of the art large wind tunnel model for active flutter suppression studies as well as the supporting techniques used in tests focused on the effects of uncertainty. Design guidelines and the resulting aeroelastic characteristics of the model are covered together with representative test results. Those would allow other researchers working in this area to develop control laws for the new model and evaluate them. A number of important lessons and insight are reported regarding the design of the model, the level of success of commonly used mathematical modelling techniques to capture its behaviour, sources of analysis / test correlation discrepancies, multi-function utilization of control surfaces for both system identification and flutter suppression, active flutter suppression testing safety, and techniques for estimating by tests of the robustness of closed-loop active aeroservoelastic systems. The new system has made it possible to repeatedly "push" the actively controlled model, using various flutter suppression control laws, safely, to the actual flutter limit in tests numerous times. This capability

---

[1] Professor, Department of Aerospace Science and Technology, AIAA senior member.
[2] PostDoc Researcher, Department of Aerospace Science and Technology.
[3] Assistant Professor, Department of Aerospace Science and Technology.
[4] Researcher, Department of Aerospace Science and Technology.
[5] Formerly PostDoc Researcher, Department of Aerospace Science and Technology, now analyst at Leonardo Helicopters.
[6] Researcher, Department of Aerospace Science and Technology.
[7] Former Professor of Aeroservoelasticity, Department of Aerospace Science and Technology
[8]. Graduate student, William E. Boeing Department of Aeronautics and Astronautics
[9]. Boeing Endowed Professor, William E. Boeing Department of Aeronautics and Astronautics, AIAA Fellow.
[10]. Professor and Chair, William E. Boeing Department of Aeronautics and Astronautics, AIAA Fellow

is just one a host of new experimental capabilities that the new system brings to the aeroelastic active control community.

Nomenclature

C	Motor damping [$Nm \cdot s$]
J	Aileron and motor inertia [$Kg \cdot m^2$]
K	Motor stiffness [$N \cdot m$]
$k_{I,0}^{p}$	0 order integral gain of the position loop
k_{P}^{p}	Proportional gain of the position loop
$k_{I,\mathrm{i}}^{v}$	I–th order integral gain of the velocity loop
k_{P}^{v}	Proportional gain of the velocity loop
m	Maximum integration order for the velocity loop
n	Maximum integration order for the position loop
s	Laplace variable
T_c	Control Torque [$Nm \cdot m$]
T_d	Torque disturbance [$Nm \cdot m$]
T_δ	Motor Torque
δ	Aileron rotation [rad]
δ_c	Aileron commanded rotation [rad]
θ	Shaft rotation [rad]
θ_c	Commanded rotation [rad]
θ_r	Reference rotation [rad]
ω	Rotational velocity
ω_r	Reference rotational velocity
ω	Frequency of oscillation [rad/s]
ω_0	Desired bandwidth
$\boldsymbol{M_{hh}}$	Generalized mass matrix
$\boldsymbol{C_{hh}}$	Generalized damping matrix
$\boldsymbol{K_{hh}}$	Generalized stiffness matrix
$\boldsymbol{U}$	Eigenvectors matrix
$\boldsymbol{q}$	Modal displacement
$\boldsymbol{H_{am}}$	Unsteady generalized aerodynamic forces matrix
k	Reduced frequency [-]
ξ_i	I-th mode damping ratio [-]
ω_{0i}	I-th mode natural frequency [rad/s]
q_∞	Dynamic pressure [Pa]
V_∞	Freestream velocity [m/s]
p	Normalized Laplace's variable
$\boldsymbol{A}, \boldsymbol{B}, \boldsymbol{C}, \boldsymbol{D}$	Generic State-Space model matrices
$\boldsymbol{x}$	State vector
$\boldsymbol{y}$	State-Space model output vector
$\boldsymbol{I}$	Identity matrix
$\boldsymbol{Q_a}$	Generalized aerodynamic forces
δ	Control surface rotation
Q_δ	Control surface hinge moment
K_δ	Actuation system stiffness
$H(s)$	Servo controller transfer function
$H_F(s)$	Shaping filter transfer function
$H_\delta(s)$	Actuator transfer function

$\boldsymbol{G}$ Gain matrix
$\boldsymbol{W_{zz}}$ Performance weight matrix
$\boldsymbol{W_{uu}}$ Input weight matrix

I. Introduction

Recent developments of the capabilities and reliability of aircraft control system hardware and software, combined with the growing structural flexibility and, hence, potential for flutter problems and for related weight reduction of optimized composite airframes, seem to have made the implementation of Active Flutter Suppression (AFS) technology more desirable and closer than ever before [1]. As noted by [1], the move from theoretical / numerical studies or studies based on highly simplified wind tunnel or flight models to full implementation of the technology requires more experimental work, in wind tunnels and in flight, using scaled models that would represent real full-size aircraft in configuration and complexity and would help identify technology deficiencies and development needs, especially from the perspective of safety and the associated uncertainty / reliability simulation and test capabilities required.

Scaled aeroelastic wind tunnel models have been used for years [2-23, also, see [1]]. Active aeroelastic wind tunnel models of real or realistic flight vehicle configurations have also been used for flutter suppression tests from the early days in which the required actuation, sensing, and control technology became practical [6-9]. Active aeroelastic wind tunnel model design and construction benefited from advancement in structural optimization [10], and in recent years the miniaturization of sensors, actuators, and computers [11], and 3D printing technology [12]. Following in the footsteps of the very few AFS tests that were carried out in the 1970s and 1980s with full-size flight vehicles [1], advances in composite material airframe construction, small sensors and actuators, and powerful on-board flight control computers have led in recent years to the development of new flight vehicles that are dedicated to AFS research: the larger X-56 UAV [13], and smaller UAVs developed by a team led by the University of Minnesota [14-18] as well as the European FlexOp project [19].

Aiming at contributing to AFS technology development and to flight vehicle active control in general, the Politecnico di Milano (POLIMI) Department of Aerospace Science and Technology (DAER) developed in the mid-2000s a scaled actively controlled aeroservoelastic model of a three-surface passenger airplane [20-21] and tested it in its large low-speed wind tunnel. With renewed interest in the testing of AFS technology – especially its design from

uncertainty aspects - using realistic large wind tunnel modes that would represent key characteristics of commonly used civil aircraft, including commercial passenger and cargo planes as well as business jets, a decision was made to base a new active aeroelastic model on the original model developed by POLIMI in the 2000s.

The paper describes the design and development of the new wind tunnel model and its systems, including the structural layout selected, the instrumentation, the process of math model refinement using ground vibration tests and wind tunnel tests, the safety features built into the model and the testing program, the multi-tasking utilization of control surfaces for both system identification (ID) and flutter suppression, the experimental techniques used to study the robustness of the control laws synthesized for the closed-loop system. The paper presents fresh findings and new insights based on the experience gained in the reported work.

The goal of the development described here is to create for the flight vehicle aeroelastic / active control community and standard case, in the public domain, that researchers will be able to use. The mathematical model of the wind tunnel model plus results of the tests carried out so far (and any future AFS tests with the wind tunnel model) will serve the AFS community for different control law synthesis and implementation strategy development and evaluation and for the comparative study of alternative techniques.

The so-called F-XDIA (XDIA for Flutter) aeroservoelastic model, where XDIA means X aircraft of Dipartimento di Ingegneria Aerospaziale, has been thoroughly modified by changing the configuration and by the addition of wind tunnel model features that would allow the study of the effects of uncertainty on the performance and reliability of AFS [22-23]. The experimental activity was divided in two main phases: the first one focused on the wing only, while the second one was dedicated to the complete model and was carried out in the POLIMI's Large Wind Tunnel. In particular, the Phase II activity was divided into two sessions: one was carried out in July 2019 and the second one in January 2020. The development successfully ended in June 2020 and led to the collection of many results concerning different flutter alleviation controllers as well robustness checks. This paper describes the whole research and development effort, with a special emphasis on the final wind tunnel results, new lessons learned, and future perspectives.

II. The F-XDIA Model: General Description

Because of its size and realistic representation (scaled) of a commercial jet, the original XDIA model [20-21] was modified to make more realistic and to modernize for the evaluation of flutter suppression technologies and the impact

of uncertainties on their performance and reliability. For this reason, the name is changed from XDIA to F-XDIA. The F-XDIA model is now a conventional jet transport configuration, with a swept-back wings and a T-Tail without the canard of the original XDIA model (see Fig. 1). The structural properties are based on those already available components and, for the newly developed components they are estimated on the basis of the manufacturing technology adopted, as briefly described in the following sections. Table 1 lists the main properties of the final wind tunnel model.

Fig. 1: Evolution of the aeroelastic XDIA wind tunnel model: the original Research Remotely Piloted Vehicle (RRPV) 1995-2005 (left), the XDIA model 2005-2012 (middle) and the F-XDIA model 2018-2022 (right).

Table 1: F-XDIA model main properties

Mass	20.8	*kg*
x_{cg}	-0.389	*m*
y_{cg}	0	*m*
z_{cg}	-0.0276	*m*
I_{xx}	4.976	kgm^2
I_{yy}	12.082	kgm^2
I_{zz}	15.658	kgm^2
I_{xz}	1.519	kgm^2
span	3.0	*m*
chord	0.25	*m*

Modal analysis of the airframe shows 20 frequencies in the range *0-45 Hz* while in terms of flutter response, the new F-XDIA model shows a classical bending torsional mode around *50 m/s*. The modified configuration of the XDIA model required the design and manufacturing of new components to replace the original ones. In the following figures the model components are sketched and briefly described.

The structural skeleton of the F-XDIA wind tunnel model is based on aluminium beams connected together. The fuselage beam is made by an aluminium tube with rectangular section. The main wing spar is built as an omega shaped aluminium beam while the horizontal and vertical tails are based on cross-shaped aluminium beams. All the structural elements are connected together by aluminium elements properly designed and milled from aluminium blocks. In the

rear part of the fuselage a single aluminium frame allows the connection together of the Tail assembly and the tail cone to the fuselage main beam (see Fig. 2).

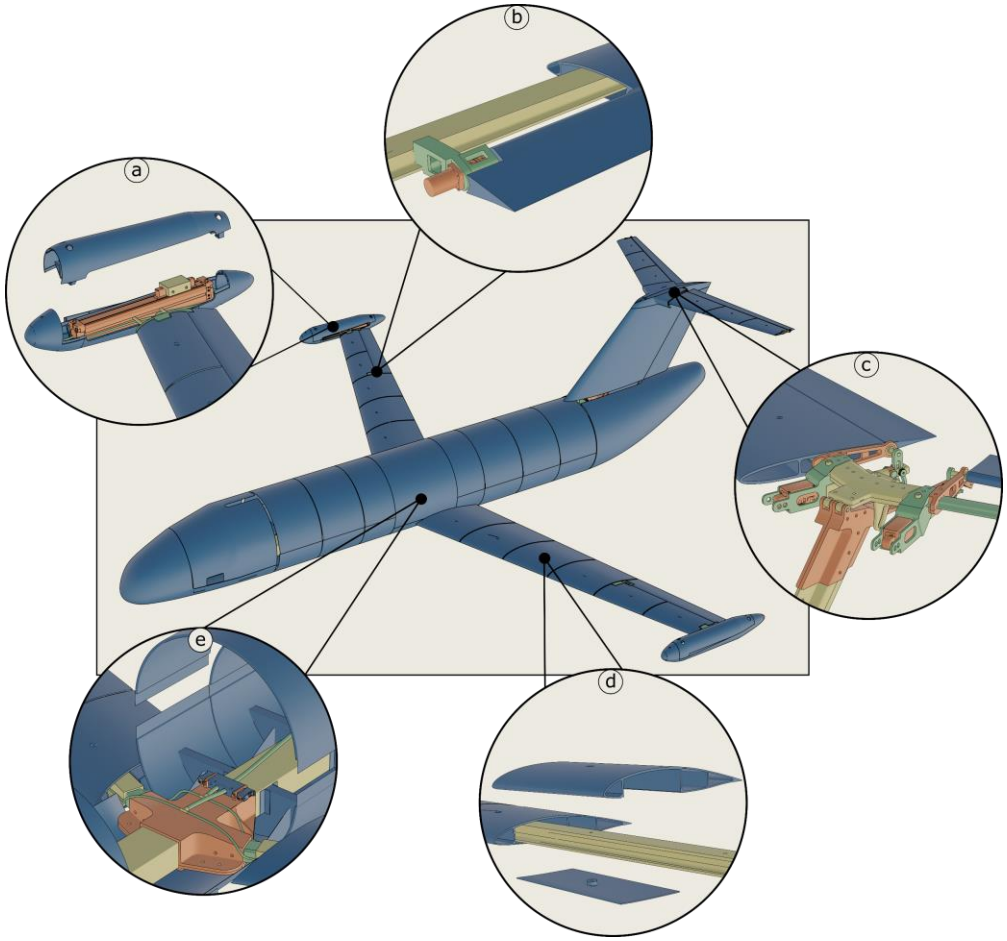

Fig. 2: The F-XDIA model and some details highlighted: the wing tip pod hosting the pneumatic actuator for the safety anti flutter mechanism (a), the aluminum rib hosting the direct connection between the electric motor and the aileron (b), the aliminum block allowing to connect the horizontal tail to the vertical tail main spa and the two linear actuators driving the elevators (c), the architecture of the 3D printed aerodynamic sectors composed by a single block connected to the spar by means of a unique bolt, together with the bottom cover (d), the central aluminum block to connect together the wing spars to the fuselage main beam (e).

The wing aerodynamic sectors are designed with two goals in mind: to guarantee the aerodynamic shapes with enough chord-wise stiffness and to allow internal space for balance masses and instrumentation installation. Since the contribution of the aerodynamic shape must be limited to its added mass without altering the stiffness distribution designed for a target aeroelastic scaling, all the aerodynamic sectors are connected to the main beams at a single span-wise location by means of a single bolt. In the case of the wing and horizontal tail the aerodynamic sectors are manufactured in one shot by 3D printing technology using a special material called WindForm™ that combines high stiffness and low mass and guarantees a very smooth external surface. The wing sectors were designed to include the

elements for the connection to the main spar and, in case of the control surfaces, the hinges and the electric drivers. The aerodynamic sectors of the vertical surfaces were already available, made from Styrofoam covered by carbon fibers. Finally, the aerodynamic sectors of the fuselage are made by honeycomb covered by carbon fibers.

A. Supporting System for Wind Tunnel Test

The F-XDIA model supporting system inside the wind tunnel consists of two vertical cables linked to the ceiling of the test chamber, plus four lateral cables installed at an angle to restrain lateral motion and serve as anti-drag, as shown in Fig. 3.

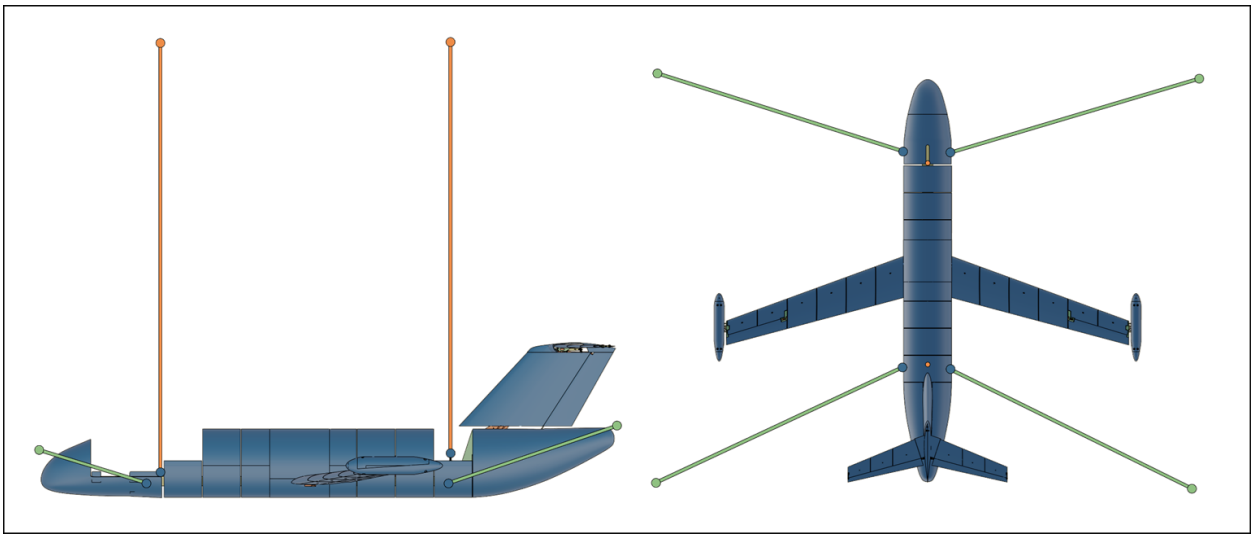

Fig. 3: Wind tunnel model supporting configuration

B. Anti-flutter Safety Device

Since the requirement for the project is to test active flutter suppression at flutter speed and beyond, a safety mechanism is required to avoid damages to the model (and, potentially, to the wind tunnel itself) in case the control law can't properly suppress the flutter. There are also some dangerous situations that can result in ineffective flutter suppression: aileron's electric motor failure, aileron's clutch failure, on-board computer crash, any failure in the feedback loop (detachment of the accelerometers from their support, cables failure), and similar.

During preliminary tests on the single half-wing inside the small wind tunnel, due to the direct access to the test chamber from the control room, a very simple and effective safety mechanism was used: a string connected to the wing tip was simply pulled and this was sufficient to stop the flutter while the wind tunnel was shutting down and the

wind speed decreases. For the final tests in the large wind tunnel with the model in a nearly free-free configuration, this solution was not applicable.

The concept of adding a flutter stopper mechanism to the model to increase its flutter speed instantaneously and save it if instability appears, has been known for years and implemented in various forms on wind tunnel flutter models [24-28]. In the work described here pneumatic circuits are used to drive the flutter stopper ballast masses to their safe locations. In the case of the DAST RPV [25] the flutter stopper consisted of just ejecting ballast masses from the wings - not a very efficient way to carry out tests. The solution adopted instead consists of movable masses at the tip of each half-wing able to quickly shift forward enough to stop the flutter mechanism when necessary: this mechanism is named flutter stopper throughout the paper.

Several flutter analyses were necessary to design the safety mechanism to understand sensitivities first, and to correctly determine the masses (both moving and fixed) later. Successive iterations were needed when existing hardware was finally selected, and fixed masses were defined. The most sensitive part of the model was found to be the wingtips. Adding masses there lowered the first bending mode frequency, separating it from the torsional mode. This required the mass to be added behind the spar (towards the trailing edge), to lower the torsional mode frequency too and allow the coalescence of those two modes so as to achieve flutter (for AFS studies) inside the wind tunnel speed envelope. Overall added mass could be too large, otherwise, it would have resulted in a very large backward positioning of the whole mechanism making the connection to the wing complex. A pneumatic actuator was finally chosen to move the mass while keeping the weight low enough.

The final pneumatic system is composed of two linear drives (one for each half-wing), one solenoid valve, and an air reservoir (both placed inside the fuselage). A proximity sensor in the rear end of each linear drive allows determining if the moving mass is in the rear or forward position and lighting a LED indicator accordingly. This feature permits a visual check from the control room of the current state of the safety system: LED ON means the mass is in the test configuration, rear position (towards the trailing edge), when flutter can occur. LED OFF means it is in the safe configuration, forward position (towards the leading edge), where flutter does not occur. The solenoid valve (FESTO, VAVG-S, bistable) is the component that selects the position of the mass. The trigger to switch it from one configuration to the other one can come in two ways: the default is that the command comes from the on-board PC when an acceleration condition at the wingtip is met. In particular, when at the same time the acceleration measured on both accelerometers on the wing tip, i.e. on LE and TE, reaches a dynamic value higher than $4g$, the flutter stop

mechanism is automatically activated. Otherwise, the emergency option allows the valve to be triggered by pushing a physical red button inside the control room, allowing the safety system to work even in case of accelerometers failures and computer crash. During the normal operation the mechanism acts pure passively as a concentrated mass. In case of too high acceleration reached at the wing tip, the mass is simply moved from rear to forward position to change the flutter mechanism. There is not any synergy between the active AFS system based on the ailerons and the flutter safety mechanism.

Linear drives (FESTO, DGC-K) shift a mass of *50 g*, the total run is *150 mm*. A *0.75 l* air reservoir (FESTO, CRVZS) is positioned inside the fuselage to supply air to the system.

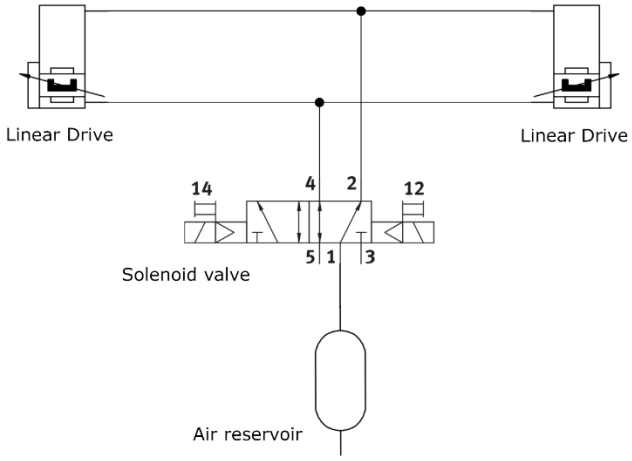

Fig. 4: Functional scheme of the safety system pressure actuator.

Tests in July 2019 and January 2020 relied on a finite air supply contained inside the model. The operating pressure at the beginning of the tests was *7 bar* and got lower after each activation of the valve. The system needed a refill when the pressure dropped below *3 bar* (meaning about six activation of the safety system). This means the wind tunnel had to be shut down and the test chamber needed to be opened. For the June 2020 test session, the system was directly connected to the wind tunnel high-pressure line, allowing a constant *8 bar* pressure with no need to periodically stop the tests to refill the reservoir.

As a result of the increased mass due to the safety system, including the actuator, the pod and all the connection system (see Fig. 5)Fig. 5: CAD Details of the anti-flutter safety device (left) and the physical one covered by the wing tip pod (right)., the predicted flutter speed was reduced to *41.5 m/s*.

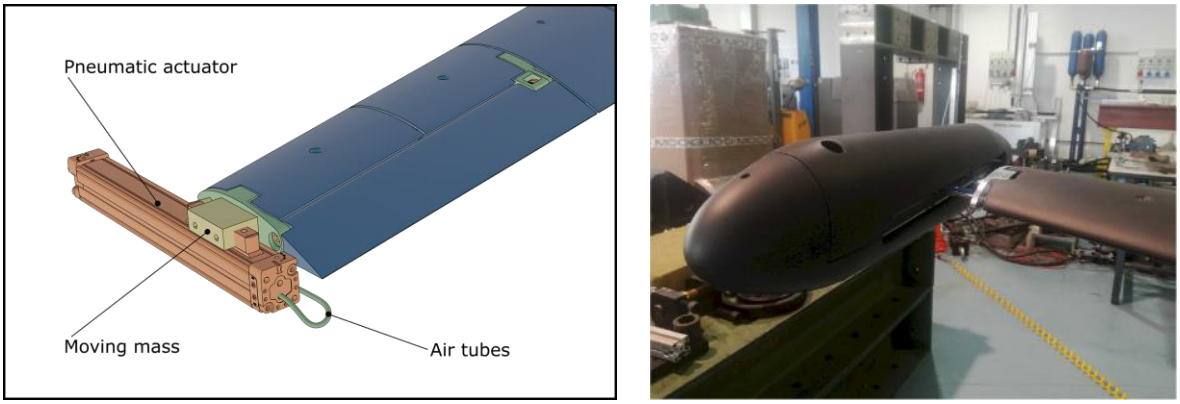

Fig. 5: CAD Details of the anti-flutter safety device (left) and the physical one covered by the wing tip pod (right).

C. Numerical Aeroelastic Model

The numerical counterpart of the physical model was realized with a Finite Element Model for the structure, coupled with a Doublet-Lattice Method model for the aerodynamics, created and solved using NASTRAN. Different numerical models were used during the entire F-XDIA project. At the beginning, the mathematical model was based on a structural stick model made of beams and concentrated masses, coupled to an aerodynamic model based on DLM approach for all the lifting surfaces. This is the typical approach adopted when the main goals of the numerical simulations are the dynamic loads or the flutter behaviour.

From the GVT of the full model and the initial correlation checks that will be described in Section III, it was evident that a pure stick model (based on classical beam theory, as commonly done in stick models) was not able to fully capture the dynamic behaviour of the wing of the wind tunnel model. The reason was identified as follows: The stiffness-driving part of the wing is made of a single aluminium spar with an omega cross shape. Due to the location of the elastic axis outside the omega section, there is a strong coupling between the in-plane and the torsional modes. Moreover, the sectional torsional properties are not fully captured using just standard beam elements, ~~probably, because of~~ due to section warping effects. For this reason, it was decided to adopt a higher fidelity finite element model. The finite element model was modified, using beam elements for the fuselage and tailplanes, plate elements for the omega-section wing spar and solid elements to model the wing-fuselage connection, as shown in Fig. 6. Using

plate elements to model the geometry of the omega spar in the hybrid model led to better analysis results / modal-test correlation.

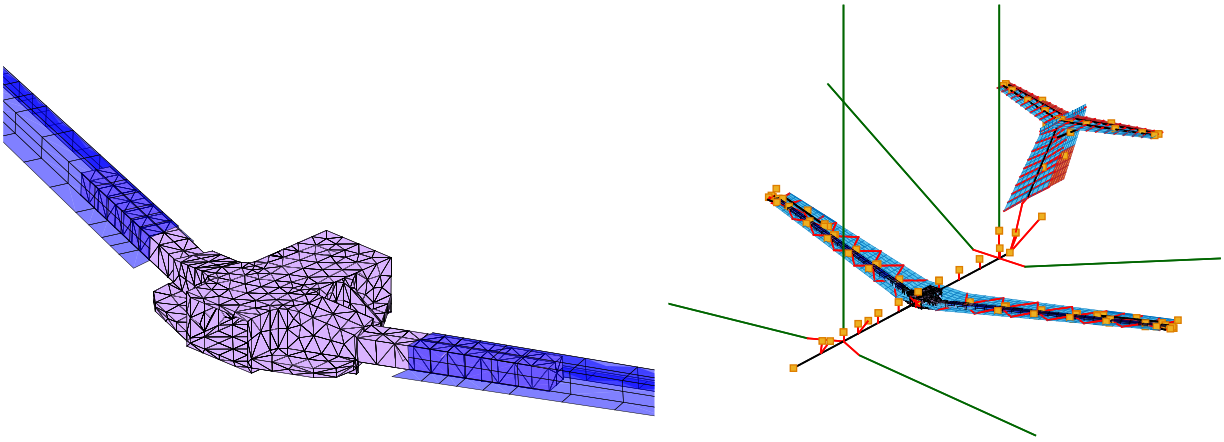

Fig. 6: Details of the wing-fuselage connection (left) and the full aeroelastic model.

In terms of aerodynamic modelling, this final hybrid model was enriched with the aerodynamic model of the tip pods that include the anti-flutter devices, modelled using the slender body theory available in NASTRAN, together with the related interference body. Despite the limitations available in modelling capability, for example only cylindrical interference bodies are possible, the effect on the flutter behaviour is not negligible. The aerodynamics of each wing sector is modelled with a dedicated CAERO1 cards, connected to a single structural point, i.e. the connection bolts of each aerodynamic sector, through a rigid element. The ailerons are modelled with a stand-alone CAERO1 panel, splined on the aileron's structural model, which is connected to the wing with a set of MPC that allows to represent the free rotation mode of the control surface, needed for the control application. The improved FEM provides a better aero-elastic correlation with the physical model, both in terms of modal parameters (shapes and frequencies) and flutter diagrams (frequency and damping).

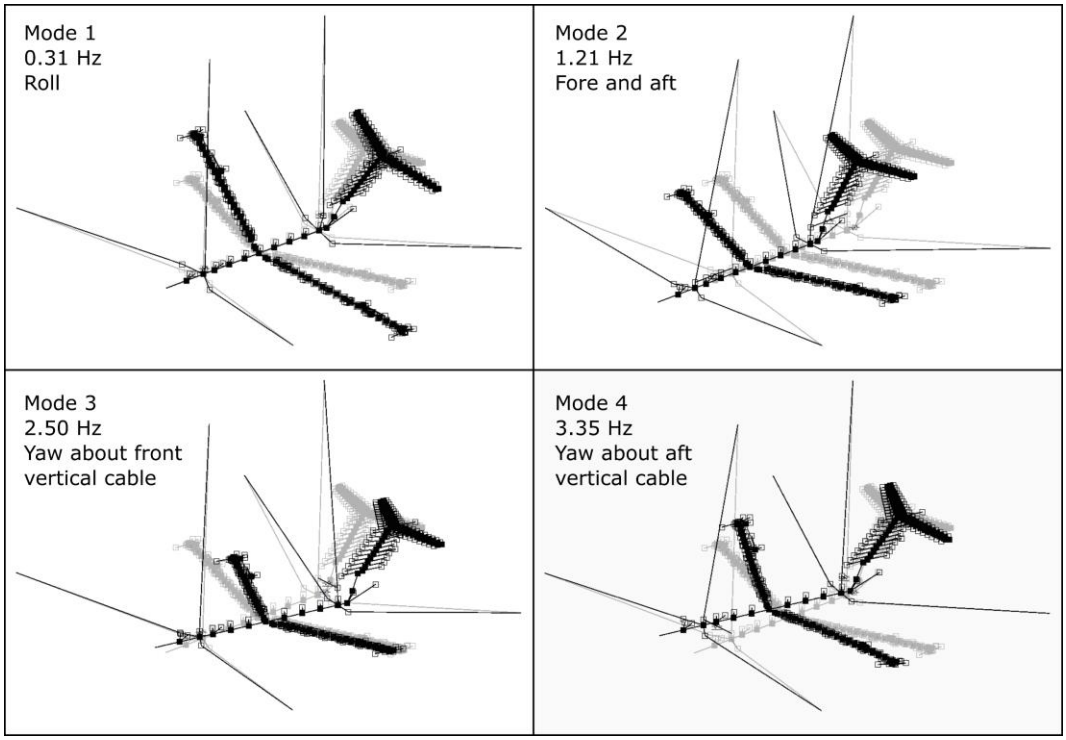

Fig. 7: The four suspension modes of the model

The supporting cables configuration affects the low-frequency dynamics of the system only, leaving the higher-frequency flutter dynamics of the free-free model, expected around *6 Hz* (see section VII), unchanged. A minimum required stiffness to prevent the occurrence of instabilities due to the coupling between the cable system and the model was estimated. As a result, steel was chosen for the vertical supporting cables, while the lateral ones were just common strings. Their stiffness was roughly determined by traction tests, just to be sure that the model on its suspension cables is above the required stability threshold.

For the finite element modelling, half of the stiffness of the lateral cables was considered to roughly take into account the fact that they can sustain traction but not compression loads without adding the complexity of non-linear analysis. This simplification is partially justified by the symmetric layout of the cables so that when one is loaded in traction, there is always a corresponding one that is loaded in compression.

An additional pendulum stiffness term Mg/L, where M is the mass fraction of the total model mass acting on the single cable, L is the length of the cable and g the acceleration of gravity, was added for both the vertical cables using spring elements. Analogous terms taking into account the same effect due to the offset between the linkage and the

elastic axis of the fuselage were directly added to the stiffness matrix using NASTRAN DMIG Direct Matrix Input. This modelling was necessary for running flutter analyses considering that additional term, which in a static analysis would be automatically added with gravity load. Table 2 and Table 3 report the properties of the cables and the resulting rigid body modes, respectively, while Fig. 7 shows the relevant mode shapes.

Overall, important lessons and insights were gained, as reported above, during the process of developing the mathematical aeroelastic model of the system regarding the FE model fidelity required for load carrying elements and for joints, the modelling of the stiffness of the cable support system, the accounting for pendulum effects of the model as a rigid body on its support cables, and the DLM modelling of the configuration with its aerodynamic strips and wing-tip flutter stopper devices.

Table 2: Properties of the suspension system elements.

Item	Young's Modulus
Steel cables	210 GPa
Common strings	6 GPa

Table 3: Numerical rigid body modes related to the suspension system.

Mode Number	Frequency
1	0.31 Hz
2	1.21 Hz
3	2.50 Hz
4	3.35 Hz

III. Experimental Activities for Model Finalization

This section describes the steps carried out to finalize the F-XDIA model before the wind tunnel test campaign. It should be noted that the steps taken to develop a reliable and useful mathematical model for the wind tunnel model and its system are identical to the steps that are required for the process of developing math models for full-size flight vehicles. The lessons and insights gained in the work described here are, thus, relevant to the math modelling processes used by industry.

A. Ground Vibration Tests (GVT)

The GVTs were not used just as final verification of the dynamic properties of the model but as a tool for tracking and identifying them and for updating the corresponding numerical models [30]. The results of the final GVT carried

out on the complete model before the wind tunnel test campaign are reported below. Two different setups were considered:

1. Setup 1: complete model, tested by hammer impact with roving method, measurements based on uniaxial low mass accelerometers (along Z direction).
2. Setup 2: only the left wing, tested by impact with fixed accelerometers method, with non-negligible sensors mass loading but with a mathematical "mass removing" technique based on the use of Modification Prediction module available in Testlab package [29] to recover out of plane and in plane motion components, and to better investigate the mode shapes.

The experimental instrumentation used during the tests was the following:

- 1 front-end SCADAS 316 for signal acquisition and conditioning;
- 28 PCB 333B32 uniaxial accelerometers, bandwidth from *0.5 Hz* to *3 kHz*, full-scale equal to *50 g*;
- 1 PCB hammer instrumented with a load cell PCB 086B03 for structural excitation. On the hammer, a soft rubber tip, a teflon tip and a metallic tip were mounted, so to excite a band up to *4 kHz*;
- Software SIEMENS-TestLab, version 17, for signal acquisition and data processing.

The GVTs were performed in two different mass distribution configurations: in both cases the aircraft was in the reference wind tunnel mass distribution but, while in the first configuration both the masses of the flutter stopper system in the wing tip pods were positioned in the forward position, in the second setup they were moved back to the rearward position. The motion of the control surfaces during the GVTs were blocked using two strips of aluminium magic band attached on the top and bottom side of the control surface gap, so without any mass or stiffness effect on the global properties of the model.

All the GVTs were carried out on the aircraft supported by the same suspension system used during the flutter tests and considering the same configuration. Moreover, the model was tested directly in the wind tunnel chamber just before the wind tunnel tests to ensure the experimental repeatability. A photo of the suspension system is shown in Fig. 8.

Fig. 8. Suspension system for GVT in wind tunnel chamber.

Table 4: GVT results.

Anti-flutter mass in forward position				Anti-flutter mass in rear position	
Mode	Frequency [*Hz*]	Damping (ς %)	Shape	Frequency [*Hz*]	Damping (ς %)
1	5.20	0.13	1st S-Bending	5.20	0.17
2	7.14	1.22	1st AS-Torsion (Left wing dominated)	7.43	1.14
3	7.78	1.08	1st S-Torsion (Right wing dominated)	7.88	0.75
4	8.26	1.03	1st htail S-Bend + 1st wing S-Bend	8.28	1.30
5	9.00	1.65	1st htail AS-Bend + 1st wing S-Bend	9.10	3.07
6	10.43	0.48	1st htail S-Bend + 1st wing S-Bend	10.38	0.39
7	12.55	1.00	1st htail S-Tors + 1st wing S-Tors	12.49	0.90
8	13.45	2.65	1st htail S-Bend	13.46	2.73
9	14.98	1.60	2nd wing AS-Bend + 2nd htail AS-Bend	14.74	1.23
10	16.36	0.83	2nd wing S-Tors + 2nd htail S-Bend	16.28	0.85
11	19.69	0.54	2nd wing AS-Tors + 2nd htail & 1st vtail AS-Bend	19.20	0.57
12	24.12	0.65	2nd wing AS-Tors + 2nd htail S-Bend	23.35	0.65

S= Simmetric, AS=Asimmetric

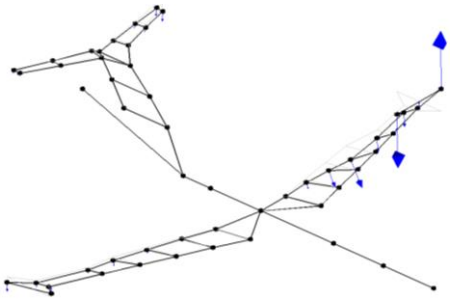

a: Mode 2, *7.14 Hz,* 1st wing torsion (Asimmetric, Left wing dominated), mass in forward position

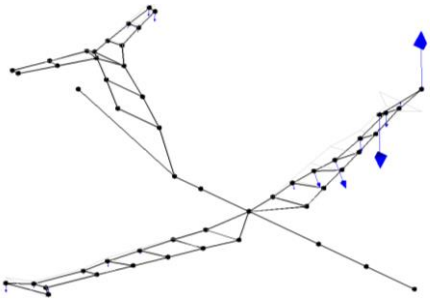

c: Mode 2, *7.43 Hz,* 1st wing torsion (Asimmetric, Left wing dominated), mass in rear position

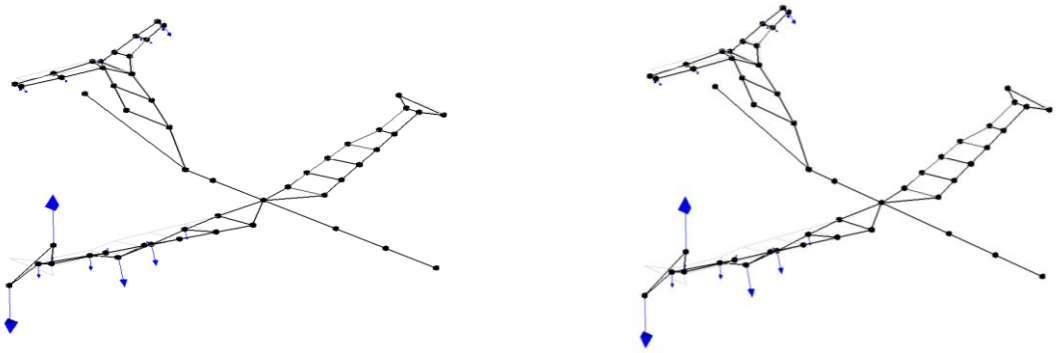

b: Mode 3, *7.78 Hz,* 2nd wing torsion (Simmetric, Right wing dominated), mass in forward position

d: Mode 3, *7.88 Hz,* 2nd wing torsion (Simmetric, Right wing dominated), mass in rear position

Fig. 9: The first two wing torsion modes: anti-flutter mass in forward position (a and b) and in rear position (c and d).

The first 12 identified modes are described in Table 4 where it is possible to see that the movement of the small mass installed on the anti-flutter device does not generate a significant changes in the modal properties of the model, despite being able to switch on and off the flutter mechanism. The 1st bending mode matches perfectly in the two cases. Concerning the torsional mode, an important aspect should be highlighted. The wind tunnel model is not perfectly symmetric, as shown in Fig. 9, therefore presenting two torsional modes at very close frequencies, with a larger participation of the left and right half wings, respectively. This is not a major surprise, considering the complexity of the wind tunnel model in terms of structural behaviour, high number of elements, large number and type of connections and different on-board instrumentations. However, since one of the goals of the project is the evaluation of the impact of the uncertainties on active flutter control technologies, it was decided to avoid seeking any artificially imposed model symmetry. It should be noted here that in some airplane designs, certain asymmetries are deliberately introduced (such as different stiffnesses between right and left engine pylons) to increase flutter speed. Configuration asymmetries are also commonly found on military aircraft carrying external stores, even in the supposedly symmetric configuration cases, due to differences in the way that external stores are attached and tightened to their pylons. In the common practice of synthesizing active flutter suppression laws for symmetric aircraft by focusing separately on the symmetric and antisymmetric cases, the possibility of asymmetric effects, as part of the modelling uncertainty involved, must be carefully considered.

B. Modal correlation and updating

Starting from the finite element model described in Section II.C and the results obtained by the GVTs, a numerical/experimental correlation improvement effort was performed. The following notes can be made:

- The 1st bending mode is captured very well in the flutter stopper mass's rear-location configuration, in terms of shape but with a frequency error of 6.9%. This is very important because the divergent flutter mechanism involves the 1st bending and the 1st symmetric torsion mode in that configuration.
- •The 1st and 2nd torsional modes are not very well captured in terms of both shape and frequency errors, equal to 7.8% and 12.8%, respectively. This is mainly due to the asymmetry of the physical wind tunnel F-XDIA model (due to manufacturing and assembly imperfections) as opposed to the numerical one that shows perfectly symmetric torsion modes.
- The adoption of the hybrid model significantly improved the correlation of both bending and torsion modes – especially in the case of the first modes that are the ones involved in flutter instability.
- Based on the GVT data, the physical model, due to the slight non-symmetry present, made it difficult to measure a single global symmetric torsion mode. There are two different torsional modes at very close frequency, related to 1st asymmetric and symmetric wing torsion, but with a larger participation of left and right wing, respectively. This generated poor correlation in the Cross-MAC matrices. For flutter suppression control law design this may justify the development of control laws that do not assume symmetry of the vehicle.

Trying to overcome these issues, two different updating processes have been developed in the form of optimization problems solved using Solution 200 of NASTRAN. In the first one, a limited number of design variables were included, related to the wing spar shape (i.e. the thickness of the horizontal and vertical walls of the omega section) and were kept constant spanwise. In the second, more aggressive optimization implementation, a larger number of design variables were introduced, including also the stiffness of the wing-fuselage connection block. More details about the two updating processes can be found in [30], and Table 5 reports the comparison between the experimental results and the numerical results after the first and the second optimization based model updating steps, of the first three modes. One important aspect must be noted here: the second model identification process required more time than what was available due to the tight calendar of the wind tunnel. The consequence was that the active flutter suppression controller was designed on the basis of a not completely correlated aeroelastic model. This in itself was

not considered a problem since the thrust of the work was to focus on active flutter suppression law synthesis in the face of uncertainty and to test the resulting laws in the wind tunnel.

Table 5. Numerical vs. experimental frequencies: comparison of optimized update_1 and optimized update_2 models.

Mode type	GVT [*Hz*]	FEM [*Hz*]	Updated_1 [*Hz*]	Updated_2 [*Hz*]
1st bending	5.20	5.59	5.55	5.27
1st Torsion (Asymmetric)	7.43	6.85	7.28	7.42
2nd Torsion (Symmetric)	7.88	6.87	7.31	7.47

IV. Data Acquisition and Control Systems

The F-XDIA wind tunnel model is equipped with two ailerons, left and right, that can be actuated in combination or separately, one elevator and one rudder. As usual in the case of wind tunnel models, the design of the actuation systems is challenging due to two main requirements: minimum size, for installation inside the wing thickness, and the allowable bandwidth, for effective control of the dynamic response. The actuation system is based on the use of electric motors supplied by Harmonic Drive. They consist of two RSF-5B supermini electric motors connected to the left and right ailerons and a RSF-11B mini electric motor connected to the rudder. (see Fig. 10). The Harmonic Drive motors are brushless actuators designed to have no backlash and ultra-precision positioning mechanism which is embedded into the patented gearbox. Both types of motors have been selected with a reduction ratio of 1:50 to produce a peak torque of *0.9 Nm*, in the case of the supermini actuator RSF-5B, and *8.3 Nm* in the case of the mini actuator RSF-11B. These three motors move the corresponding control surfaces through a direct transmission consisting of elastic joints and they are driven by the proprietary HA-680 drivers which are used in torque control mode. The actuators are equipped with an embedded encoder enabling a direct measurement of the rotation which can be used inside a servo-control loop. For the ailerons and the rudder, a dual loop servo-controller was designed and adopted aiming at the possibility of introducing a maximum bandwidth of *15 Hz*, around double of the expected flutter frequency, and the nonlinear saturations typical of full-scale aircraft actuators. In the case of the elevator, a different solution was adopted, based on a single Actuonix L-16 linear actuator which rotates each elevator through a pivot able to slide inside a curved guide, as shown in Fig. 2. This kind of actuation system shows a limited bandwidth, but this is not considered a limitation since no active control laws based on the use of elevators were foreseen in the project.

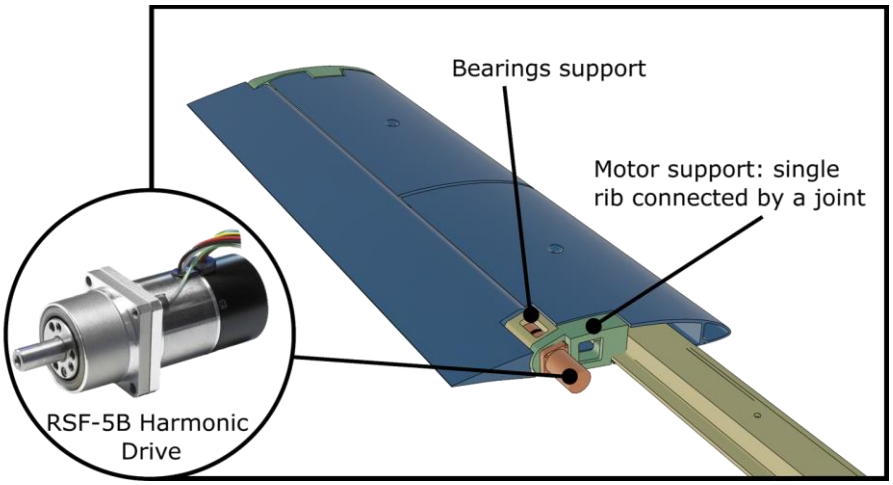

Fig. 10: The RSF-5B Harmonic Drive used to control the ailerons.

The aileron rotation command comes from the active control system, as described in Section V, which uses sensors installed on the F-XDIA model. The main sensors are MEMS accelerometers by PCB which provide good accuracy at low frequencies. However, they were selected mainly because their pre-amplified channels can be read by a standard data acquisition system without the need of expensive and heavy IEPE modules, usually adopted in the case of piezo-electric accelerometers. This choice allows for a small, embedded computer to be installed inside the wind tunnel model to manage the test in terms of acquisition and active control duties. The embedded computer is equipped with the in-house developed Real Time Application Interface (RTAI) [31], based on the Linux operating system. The on-board computer, as well as all the acquisition system, is based on the PC-104 form factor allowing for a final small size and weight system embedded into the wind tunnel model, as shown in Fig. 11, while the location of the accelerometers used by the control system over the model are sketched in Fig. 12.

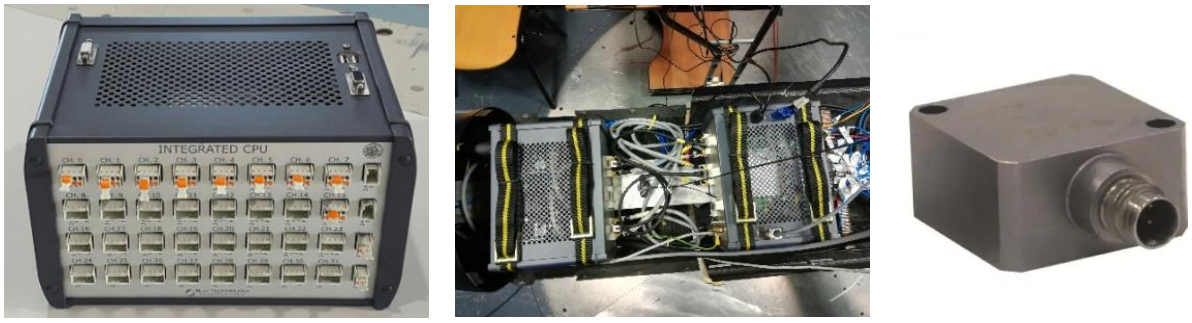

Fig. 11: The dedicated onboard computer equipped with all the requested I/O cards (left) and the complete hardware inside the fuselage (center); one of the MEMS accelerometers installed on the model (right).

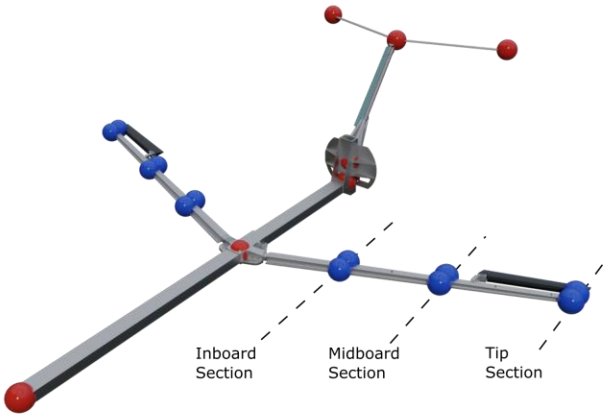

Fig. 12: The accelerometers locations over the model: blue dots mean accelerometers used for control, while red dots indicate accelerometers used for identification.

A. The servo-control system for ailerons

Aircraft are typically equipped with electro-hydraulic actuators embedding various internal non-linearities, such as force and rate saturations [32]. On the other hand, wind tunnel models are usually equipped with small electrical motors due to the constrained size, and this is also the case of the F-XDIA model. The electrical motors present some rate saturation, but at values that are not in the range of interest, and they have a torque saturation, but it is related to the maximum current that can be applied to the motor. In order to reproduce the typical electro-hydraulic actuator performances, combining maximum rotation velocity and actual dynamic response, a specific control law is here adopted, based on the dual loop servo controller initially proposed in [32] and then extended to a more general formulation [33]. The scheme of the controller is sketched in Fig. 13.

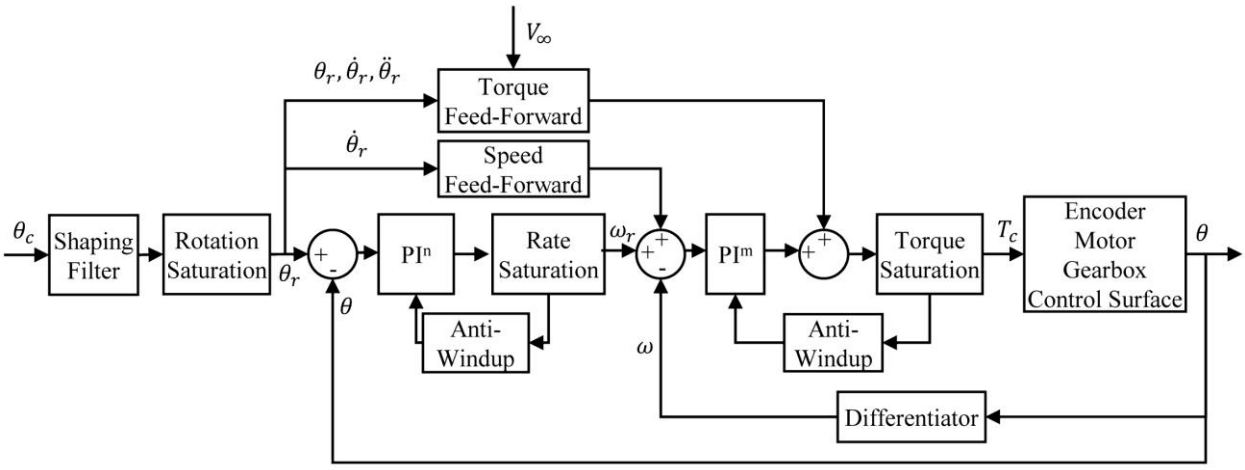

Fig. 13: The adopted control scheme for the ailerons.

While the inner control loop makes the actuator sufficiently fast to follow abrupt speed changes, e.g. possible rate saturations, the output control loop assures the desired positioning accuracy within the required bandwidth, that is *15 Hz* in this case. The elastic joint connecting the motor to the aileron is adequately stiff to ensure an acceptable separation of the mode frequency of the two connected masses (around *90 Hz*) with respect to any foreseeable control bandwidth. The motor-aileron set-up was, therefore, modeled as a single rigid degree of freedom system, simply dubbed the motor. The equations of motion of the motor, can be cast in the Laplace transform domain, as:

$$\left(Js + C + \frac{K}{s}\right)\omega = T_c + T_d \tag{1}$$

$$(Js^2 + Cs + K)\theta = T_c + T_d \tag{2}$$

with $\omega = s\theta$ and T_c and T_d are the Torque control and disturbance, respectively. It should be remarked that J, C, K can comprise also the contributions related to a quasi steady approximation of the aileron hinge moment associated to the flow. Thus they are dependent on the free wind stream dynamic pressure. Due to the need of taking into account possible constraints imposed on T_c, ω and θ the servo is designed using a dual velocity-rotation control loops. Thus T_c is first servoed to a velocity reference ω_r, inner loop, which is the rotation error $(\theta_r - \theta)$, outer loop. The inner and outer loops are structured as a proportional plus arbitrary order integral gains, as synthesized by the notations $(P * I^m)_\omega$ and $(P * I^n)_\theta$, for the inner and outer loop respectively. The related equations adopted in this work are:

$$\omega_r = k_{I,0}^p(\theta_r - \theta) \tag{3}$$

$$T_c = \frac{k_{I,m}^v}{s^m}\omega_r - \left(k_P^v + \frac{k_{I,1}^v}{s} + \sum_{i=2}^{m}\frac{k_{I,i}^v}{s^i}\right)\omega \tag{4}$$

where m = 4, n has been set to 0 and, as an important remark, the indices 0 imply $k_{I,0}^p = k_P^p$ and $k_{I,0}^v = k_P^v$. The only sensed variable, through an incremental encoder, is θ, ω being obtained by a numerical differentiation, with a step varying in relation to the the motor rotational speed.

Moreover, it should be pointed out that the bandwidth of the torque controller, i.e. the driver current loop, is in the range of a few *kHz* and thus needs not to be modeled.

The above equations can be combined in a single equation driven only by the reference rotation command θ_r. Whatever are the position loop gains, velocity loop gains from $i = 2$ upward, will make the motor completely insensitive to the variations of its nominal inertia, damping and stiffness parameters. More details on the new dual loop formulation can be found in [33].

B. Design of the servo controller

The adopted design technique is based on standard closed loop pole assignment matching a desired transfer function with little or no overshoot. Once the order, n and m, of the integral terms has been chosen the transfer function will be of the kind:

$$H(\mathrm{s}) = \frac{a_0}{s^{n+m+2} + a_{n+m+1}\ s^{n+m+1} + a_{n+m}\ s^{n+m} + \cdots + a_1\ s + a_0} \tag{5}$$

It is then possible to assign the values of the denominator coefficients on the base of the desired prototype transfer function.

The choice of the prototype transfer function, i.e its denominator of order $(m + n + 2)$, is not unique. So our specification was based on assigning the 3dB closed loop bandwidth, say ω_0, and a polynomial structured for a null, or almost negligible, overshoot for the step response of the rotation and velocity.

A simpler and viable choice could be the simpler $(s + a)^{m+n+2} = 0$, which has been the one adopted in our project, with $m = 4$ and $n = 0$, $\omega_0 = 15\ \ (Hz)$ and the design was carried out on the base of J, i.e. with C and K set to zero. The controller design was carried out considering only what is known and fixed during the tests, that is the

motor inertia J. The other two quantities C and K depends on the dynamic pressure that is variable during the wind tunnel tests. They could be scheduled or not considered during the design. In this work, the second way was preferred after verifying that the servo-controller is adequately robust.The desired bandwidth is divided by the coefficient $s_f = 0.3493$, as is usually done for converting filter parameters to achieve 3dB at the design bandwidth. For the nominal system, the above PI^4PI^0 design achieves the following:

1. 3 dB velocity bandwidth of 44.3 (Hz)

   (a) Phase Margin (PM) 66 deg, Gain Margin (GM) 0.33

   (b) Vector Gain Margin (VGM) 1.092430, -10.818946 ≤ GM ≤0.48, PM ≥ 66 deg;

2. 3 dB rotation bandwidth of 15.0 (Hz) [3 dB phase -110 (deg)]

   (a) PM 66 deg, GM 3.4

   (b) VGM 1.078386, -12.8 ≤ GM ≤ 0.48, PM ≥ 65 deg

Its discretized implementation was set at *1500 Hz*, which may look a higher than needed. It should be taken into account that the command of the active flutter controller were set at a rate of a few hundred *Hz*. Thus, a fast sampling of the servo commands was needed to avoid adding undue delays to the faster and unsynchronized flutter suppression commands. Moreover, the capability of compensating bounded disturbances up to the third order has made is unnecessary to schedule the servo gains at varying dynamic pressure, from 0 to *1600 Pa*.

A feed-forward could be applied at the ω_r and T_c input, the latter being chosen as an optional choice in our case:

$$T_f = \beta \cdot (Js^2 + Cs + K) \cdot \theta_r \tag{6}$$

with β being a scaling factor and T_f the Torque feed-forward.

When combined with a controller having an adequate stability robustness, a feed-forward with J, C, and M changing against a varying dynamic pressure can provide some kind of adaptation. With that said, after a few test checks this showed no sinificant improvement and it was not used.

V. State-Space model and control implementation

The numerical model of the wind tunnel demonstrator is realized in NASTRAN (FEM + VLM/DLM aerodynamics) and it needs to be transformed in a more compatible format for the study and development of active

flutter suppression control logics. The numerical model is also important to assess the capability of the available numerical tools to accurately predict the aeroelastic system dynamics, its sensitivity to the change of model parameters (wind tunnel speed, mass configuration, aerodynamic surface configuration) and the effectiveness of the flutter suppression system.

The model must include the structural dynamic description of the wind tunnel model, as well as its coupling with unsteady aerodynamic forces. Since the model will be mainly used in conjunction with control systems, it must also include the definition of system inputs, that is actuator rotation commands, and of the system outputs, that is the measurements obtained through the sensors distributed on the structure. The details on how the model dynamics, inputs and outputs are defined is given in the following

A. Model dynamics

The aeroelastic system model is based on the availability of a NASTRAN FEM model that includes the definition of structural properties, the aerodynamic surfaces (aerodynamic mesh), and the coupling between structural and aerodynamic models (spline elements). The numerical model includes the definition of the suspension system, consisting in a set of cables modeled using rod elements. It also includes the definition of the control surfaces, modelled as structural elements with the actual geometry, mass properties and hinge mechanism. The control surfaces hinges are defined to allow the free rotation of the surface, thus leaving the free surface rotation rigid mode in the model.

The aero-structural matrices are extracted from NASTRAN with the ALTER [34] technique and processed in Matlab with NeoCASS [35-36-37-38], this procedure is repeated for both fixed and free control surfaces.

The information needed to assemble the dynamic model are:

- The **U** matrix which contains the modal shapes and its sizes are nDofs x nModes.
- The generalized mass $\mathbf{M_{hh}}$, stiffness $\mathbf{K_{hh}}$and damping $\mathbf{C_{hh}}$ matrices associated with the reduced basis **U**;
- The unsteady generalized aerodynamic force matrices $\mathbf{H}_{am}(k)$ associated to the reduced basis **U** and tabulated according to the reduced frequency $k = \frac{f\, l_{ref}}{V_\infty}$ (since the wind tunnel is operating at low speed, no Mach variation is considered, but just the value of Mach=*0.1* has been considered).

The aero-structural matrices are extracted while performing a flutter analysis (SOL 145). The aeroelastic system dynamics can then be expressed through the Laplace's transformation as in Eq.(7):

$$(\mathbf{M_{hh}}s^2 + \mathbf{C_{hh}}s + \mathbf{K_{hh}} - q_\infty \mathbf{H}_{am}(k))\mathbf{q} = \mathbf{Q} \tag{7}$$

where $\mathbf{Q}$ represents a generic generalized modal force input. The structural damping can be obtained assuming a proportional damping of the type $c_i = 2\,\xi_i \omega_{0i}^2 m_i$, leading to the strucural matrices in the form of Eq.(8):

$$\mathbf{M_{hh}} = \begin{bmatrix} \ddots & & \\ & \mathrm{m_i} & \\ & & \ddots \end{bmatrix}; \mathbf{C_{hh}} = \begin{bmatrix} \ddots & & \\ & \mathrm{c_i} & \\ & & \ddots \end{bmatrix}; \mathbf{K_{hh}} = \begin{bmatrix} \ddots & & \\ & k_i & \\ & & \ddots \end{bmatrix} \tag{8}$$

In this formulation, the Generalized Aerodynamic Forces (GAFs) are the output of a transfer function where the input is the modal displacement $\boldsymbol{GAFs}(k) = q_\infty \boldsymbol{H_{am}}(k)\boldsymbol{q}(k)$, the transfer function is known for a given set of reduced frequencies. To obtain a State-Space representation of the problem, the $\boldsymbol{GAFs}$ must be translated into the time domain. This is done following the Matrix Fraction Approximation (MFA) approach described in [39] and implemented in NeoCASS. The aerodynamic transfer function matrix $\boldsymbol{H_{am}}(p)$ is approximated in the form of Eq.(9), where $p = \sigma + jk$ is the normalized Laplace variable and $\boldsymbol{A_a}, \boldsymbol{B_a^i}, \boldsymbol{C_a}, \boldsymbol{D_a^i}$ are the matrices identified with the MFA approach.

$$\mathbf{H}_{am}(p) \approx \mathbf{D^0}_a + p\mathbf{D^1}_a + p^2\mathbf{D^2}_a + \mathbf{C}_a(p\mathbf{I} - \mathbf{A}_a)^{-1}(\mathbf{B^0}_a + p\mathbf{B^1}_a + p^2\mathbf{B^2}_a) \tag{9}$$

The identified matrices are used to assemble the dynamic State-Space (SS) model that represents the aerodynamic system, having the modal coordinates as input and the generalized aerodynamic forces as output.

$$\begin{cases} \dfrac{d\mathbf{x}_a}{dt} & = \dfrac{1}{t_a}\mathbf{A}_a\mathbf{x}_a + \dfrac{1}{t_a}\mathbf{B^0}_a\mathbf{q} + \mathbf{B^1}_a\dot{\mathbf{q}} + t_a\mathbf{B^2}_a\ddot{\mathbf{q}} \\ \mathbf{Q_a} & = \mathbf{C}_a\mathbf{x}_a + \mathbf{D^0}_a\mathbf{q} + t_a\mathbf{D^1}_a\dot{\mathbf{q}} + t_a^2\mathbf{D^2}_a\ddot{\mathbf{q}} \end{cases} \tag{10}$$

The SS-system of Eq. (10) is coupled to the mechanical SS-model, providing the coupling between the elastic and aerodynamic system and creating the full aero-elastic system in time domain, as described in Eq.(11)

$$\begin{bmatrix} \mathbf{I} & \mathbf{0} & \mathbf{0} \\ \mathbf{0} & \mathbf{M} - q_\infty t_a^2\mathbf{D^2}_a & \mathbf{0} \\ \mathbf{0} & -t_a^2\mathbf{B^2}_a & t_a\mathbf{I} \end{bmatrix} \frac{d}{dt}\begin{bmatrix} \mathbf{q} \\ \dot{\mathbf{q}} \\ \mathbf{x}_a \end{bmatrix} = \begin{bmatrix} \mathbf{0} & \mathbf{I} & \mathbf{0} \\ -(\mathbf{K} - q_\infty\mathbf{D^0}_a) & -(\mathbf{C} - q_\infty t_a\mathbf{D^1}_a) & q_\infty\mathbf{C}_a \\ \mathbf{B^0}_a & t_a\mathbf{B^1}_a & \mathbf{A}_a \end{bmatrix}\begin{bmatrix} \mathbf{q} \\ \dot{\mathbf{q}} \\ \mathbf{x}_a \end{bmatrix} + \begin{bmatrix} \mathbf{0} \\ \mathbf{Q} \\ \mathbf{0} \end{bmatrix} \tag{11}$$

The aeroelastic SS system can be re-written in a compact form as in Eq.(12)

$$\bar{\mathbf{E}}\dot{\mathbf{x}}_{ae} = \bar{\mathbf{A}}\mathbf{x}_{ae} + \bar{\mathbf{f}} \tag{12}$$

B. Input definition

The aeroelastic system of Eq.(12) has as input the generalized modal forces. The wind tunnel model is commanded entirely by forcing the aileron rotation by means of electric motors. In order to model the system response to such input it is necessary to define the generalized modal forces associated with the torque that the motors are applying on the aileron shaft. The aileron kinematics is already defined in the model description and the aileron rotation δ is defined in term of modal coordinates as in Eq.(13).

$$\delta = \mathbf{U}_{\boldsymbol{\delta}}\boldsymbol{q} \tag{13}$$

The relation between $\boldsymbol{\delta}$ and $\mathbf{q}$ is generic, making use of the full $\mathbf{U}$ modal basis matrix and for generality does not rely on the presence of the explicit control surface rotation modes in the modal basis.

The control surface hinge moment is the load energetically conjugated with the surface rotation, it then can be expressed as

$$\mathbf{Q}_{\boldsymbol{\delta}} = \boldsymbol{U}_{\boldsymbol{\delta}}^{T}\boldsymbol{T}_{\boldsymbol{\delta}} \tag{14}$$

Eq.(14) leads to the input definition of Eq.(15).

$$\bar{\mathbf{f}} = \begin{bmatrix} \mathbf{0} \\ \mathbf{U}_{\delta}^{T} \\ \mathbf{0} \end{bmatrix} \mathbf{T}_{\delta} = \bar{\boldsymbol{B}}_{\delta}\boldsymbol{T}_{\delta} \tag{15}$$

Generally, it is preferable to have an aileron deflection command as system input instead of the motor torque $\boldsymbol{T}_{\boldsymbol{\delta}}$. This simplifies the design of control laws and provides a more intuitive way to control the wind tunnel model. The possibility to control the aircraft using a commanded control surface deflection is also more representative of the configuration of most of the current large transport aircraft that are equipped with hydraulic actuators.

In the case of F-XDIA model, as explained in paragraph IV, there is an elastic joint connecting the motor shaft to the aileron. Since the aileron is positioned using the encoder embedded in the motor the designed servo is co-located with its sensor and not with the aileron, so that there remains a slight inaccuracy in matching the commanded aileron rotation, in the order of one tenth of degree at the saturated motor torque. In such a view, in the simulations verifying the various active controllers, the actuating system is then modelled as shown in Fig. 14.

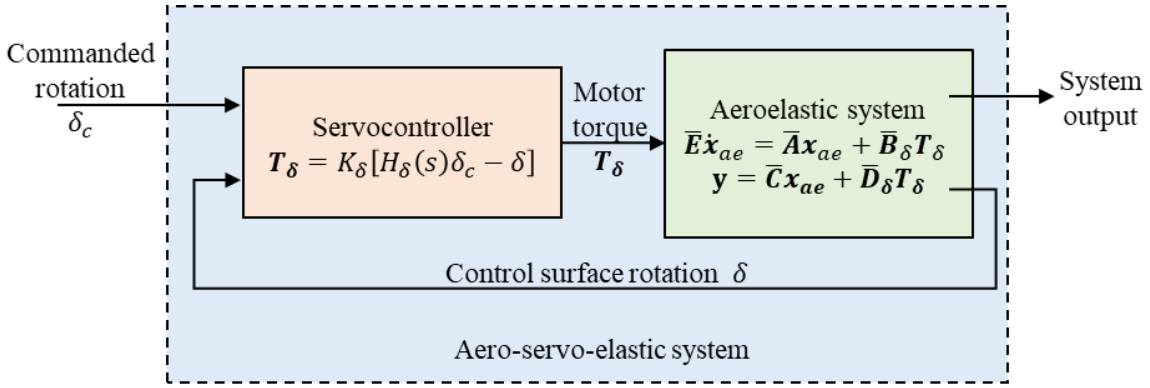

Fig. 14: Interconnection between the aeroelastic model and the servo controller

From Fig. (14), it can then be seen that such a model takes into account the joint stiffness K_δ, the two halves of its inertia being lumped at the motor shaft and aileron and thus hidden in $H_\delta(s)$ and in the aeroelastic model respectively. Therefore, the effect of the joint compliance on the commanded aileron deflection is thus explicitly given by

$$\delta = H_\delta(s)\delta_c - \frac{1}{K_\delta}T_\delta \tag{16}$$

with $H_\delta(s) = H_F(s) \cdot H(s)$, $H_F(s)$ being the transfer function of the command shaping filter. The design of the control system for the actuator and the definition of its transfer function are presented in section IV.B. The interconnection between the servo controller and the aeroelastic model is shown in Fig. 14. The servo controller acts as an interface between the desired rotation and the actual aeroelastic model, it also provides a stiffness contribution for the aileron degree of freedom. The feedback connection of the servo controller and the aeroelastic system constitutes the aeroservoelastic system.

A separate system must be defined for each aileron, and can be reformulated in State-Space form considering a controllable canonical form for $H_\delta(s) = \frac{\sum_{i=0}^{nN} n_i s^i}{\sum_{i=0}^{nD} d_i s^i}$ with nN $<$ nD:

$$\begin{cases} \dot{\boldsymbol{x}}_{\boldsymbol{\delta}} & = \begin{bmatrix} \mathbf{0}_{nD-1\ x\ 1} & \boldsymbol{I}_{nD-1\ x\ nD-1} \\ \dfrac{-d_0}{d_{nD}} & \dfrac{-d_{nD-1}}{d_{nD}} \end{bmatrix} \boldsymbol{x}_{\boldsymbol{\delta}} + \begin{bmatrix} \mathbf{0}_{nD-1\ x\ 1} & \mathbf{0}_{nD-1\ x\ 1} \\ \dfrac{1}{d_{nD}} & 0 \end{bmatrix} \begin{bmatrix} \delta_c \\ \delta \end{bmatrix} \\ T_\delta & = [K_\delta + n_0 \quad \mathrm{n}_N] x_\delta + [0 \quad -K_\delta] \begin{bmatrix} \delta_c \\ \delta \end{bmatrix} \end{cases} \tag{17}$$

The system is actually obtained introducing a coupling with the aeroelastic system described in Section A, due to the fact that the input δ of the servo-controller system is an output of the aeroelastic system, while the output T_δ is an input of the aeroelastic system.

By collecting the servo-system models for the two ailerons it is possible to write the system in the more compact form of Eq.(18).

$$\begin{cases} \dot{\mathbf{x}}_\delta & = \mathbf{A}_\delta \mathbf{x}_\delta + \mathbf{B}_{\delta_c} \boldsymbol{\delta}_c + \mathbf{B}_\delta \boldsymbol{\delta} \\ \mathbf{T}_\delta & = \mathbf{C}_\delta \mathbf{x}_\delta + \mathbf{D}_{\delta_c} \boldsymbol{\delta}_c + \mathbf{D}_\delta \boldsymbol{\delta} \end{cases} \tag{18}$$

The $\boldsymbol{T}_{\boldsymbol{\delta}}$ and $\boldsymbol{\delta}$ allows coupling of the servo-controller with the aero-elastic SS model, creating the full aero-servo-elastic model of the aircraft, with the state $\mathbf{x} = [\mathbf{q}^T, \dot{\mathbf{q}}^T, \mathbf{x}_a^T, \mathbf{x}_\delta^T]^T$ and the input $\boldsymbol{\delta_c}$.

$$\hat{\mathbf{E}}\dot{\mathbf{x}} = \hat{\mathbf{A}}\mathbf{x} + \hat{\mathbf{B}}\boldsymbol{\delta}_c \tag{19}$$

For the system described by Eq. (19) the output definition is still missing and will be treated in the next section. The system is formulated in the descriptor form, with the $\hat{\mathbf{E}}$ matrix multiplying the derivative of the state, an inversion of this matrix can be used to get the model in the conventional explicit form of Eq.(20), where $\mathbf{A} = \hat{\mathbf{E}}^{-1}\hat{\mathbf{A}}$, $\mathbf{B} = \hat{\mathbf{E}}^{-1}\hat{\mathbf{B}}$.

$$\dot{\mathbf{x}} = \mathbf{A}\mathbf{x} + \mathbf{B}\boldsymbol{\delta}_c \tag{20}$$

C. Output definition

The output of the system, used both for model correlation and sensing and control are the accelerations measured at several locations distributed on the structure as in Fig. 11 and the control surfaces' rotation. For each measurement location (and measurement direction) the acceleration can be defined on the numerical model starting from the knowledge of the modal basis and the modal acceleration, the acceleration on the $i-th$ location will be computed as:

$$\begin{bmatrix} a \\ \delta \end{bmatrix} = \begin{bmatrix} \boldsymbol{U_a} & 0 \\ 0 & \boldsymbol{U_\delta} \end{bmatrix} \begin{bmatrix} \ddot{\boldsymbol{q}} \\ \boldsymbol{q} \end{bmatrix} \tag{21}$$

and the full set outputs' set:

$$\mathbf{y} = \widetilde{\boldsymbol{U}}\widetilde{\boldsymbol{q}} \tag{22}$$

The definition of the acceleration can readily be applied to the definition of the state of the aeroservoelastic system as in Eq.(23) while the control surface rotation is defined by Eq.(13).

$$\mathbf{a} = [\mathbf{0} \quad \mathbf{U}_a \quad \mathbf{0} \quad \mathbf{0}]\dot{\mathbf{x}} \tag{23}$$

The output definition leads to the classical representation of the SS form of Eq.(24)

$$\begin{cases} \dot{\mathbf{x}} & = \mathbf{A}\mathbf{x} + \mathbf{B}\boldsymbol{\delta}_c \\ \mathbf{y} & = \mathbf{C}\mathbf{x} + \mathbf{D}\boldsymbol{\delta}_c \end{cases} \tag{24}$$

Where the $\boldsymbol{C}$ and $\boldsymbol{D}$ matrices are defined by Eq.(25)

$$\boldsymbol{C} = \begin{bmatrix} [\mathbf{0} & \mathbf{U}_a & \mathbf{0} & \mathbf{0}]\mathbf{A} \\ [\mathbf{U}_\delta & \mathbf{0} & \mathbf{0} & \mathbf{0}] \end{bmatrix} \text{ and } \boldsymbol{D} = \begin{bmatrix} [\mathbf{0} & \mathbf{U}_a & \mathbf{0} & \mathbf{0}]\mathbf{B} \\ & \mathbf{0} & & \end{bmatrix} \tag{25}$$

D. State-Space model in Simulink

Finally, it was possible to assemble a State-Space model of the aircraft where the inputs are the control surfaces deflection required by the controller and the outputs are the measures needed by the controller and the one logged for monitoring purpose. The general Simulink model is represented in Fig. 15 , where in the AFS controller block $\boldsymbol{G}(\boldsymbol{s})$ indicates an arbitrary transfer function for the control law, which considers eventual filtering and integration on the measures.

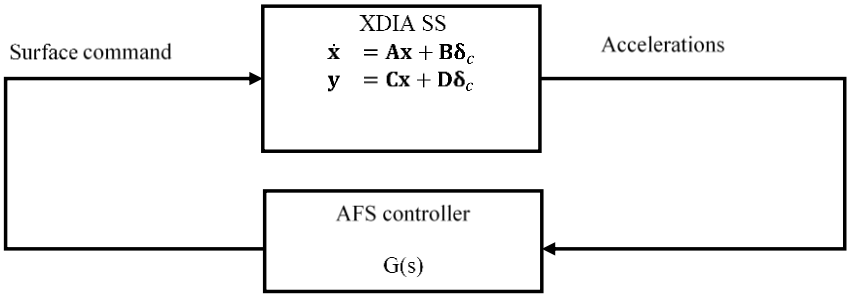

Fig. 15: General Simulink scheme of the AFS controller

The full aero-servo-elastic Simulink model, used to synthesize the active suppression flutter controllers is shown in Fig. 16, where additional features are implemented: a wash-out high pass filter is added to remove the static component of the MEMS accelerometer, together with their transfer functions.

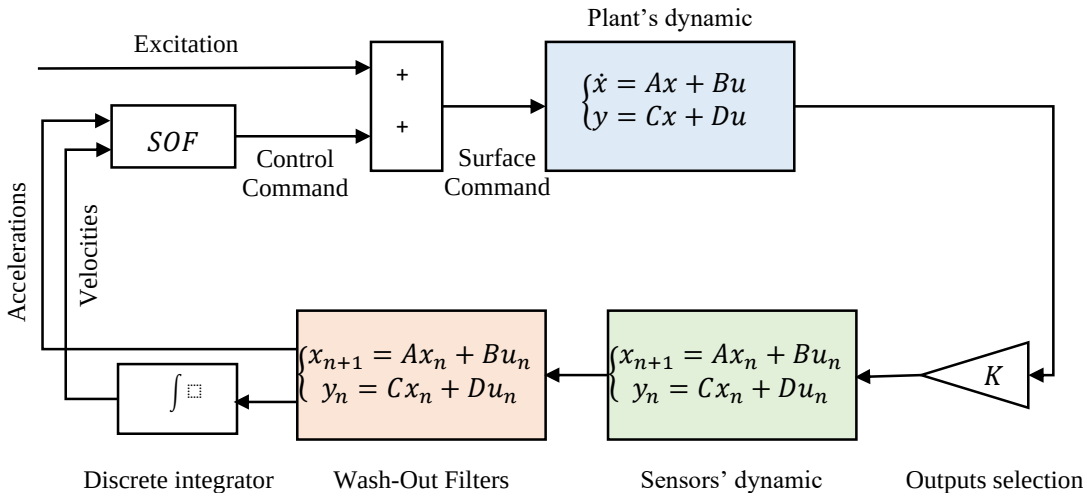

Fig. 16: Simulink model specialized for the SOF controller architecture

VI. Active Flutter Suppression Strategies

Different kinds of controllers for flutter suppression were developed, and the experimental campaign described here was aimed at collecting enough data to study all of them in action. It should be noted that the synthesis and evaluation of these laws are considered exploratory, since the wind tunnel model and capabilities described here will,

hopefully, lead to the experimental evaluation in the future of many flutter control strategies. In detail, three types of controllers were developed and tested in the wind tunnel so far:

- SOF Static Output Feedback. Time domain control theory, based on optimal strategy. The control input u is linearly proportional to the measurements $\{y\}$, providing so a direct control gain matrix, without introducing any delays (No undesired dynamics are involved. This is a static controller).
- ILAF: Identical Location of Acceleration and Forces. Integrating structural acceleration at one point, the ILAF system works to create a velocity-proportional force in direction opposite to the structural velocity at the same point. This force being opposite to the speed creates an effective viscous damper for the structure. The key issues are: Identical location of accelerometer and force and approximate integration of acceleration to obtain velocity signal.
- LQG Linear–quadratic–Gaussian control. Time domain control theory, based on optimal control. An LQG controller is a combination of a Linear Quadratic Estimator (LQE) together with a Linear Quadratic Regulator (LQR). The LQE is a Kalman filter. This type of controller is widely known and widely studies.

Because of the focus of the present paper on the innovations involved in and the details of the new wind tunnel system for AFS research, exploratory results with only the SOF controller are presented here, while details about the other controllers and their performances can be found in [40].

A. Static Output Feedback (SOF)

Static Output Control (SOF) [41] is a simple and effective approach to aeroservoelastic control law synthesis that has been already studied and proven successful for active flutter suppression (AFS) and gust load alleviation (GLA) [42], [43], [44]. In the implementation of Static Output Feedback (SOF), the control input, $\boldsymbol{U}(s)$, is obtained from measured responses, $\boldsymbol{Y}(s)$, by means of a constant gain matrix, $\boldsymbol{G}(s)$, as $\boldsymbol{U}(s) = \boldsymbol{G}(s)\,\boldsymbol{Y}(s)$. The behavior of the controller is then defined by the values of the elements of the gain matrix, which are computed by minimizing a weighted H_2 norm of the closed loop system.

To properly identify the closed loop transfer function whose norm is to be minimized, it is necessary to identify the performance output of interest, $\boldsymbol{z}$, that is the set of system outputs whose responses need to be reduced. For example: the internal loads in the structure in the case of a GLA controller. To obtain a well-posed optimization

problem, it is necessary also to include the controller input, $\boldsymbol{U}$, in the list of outputs included in the norm of the closed loop system. The closed loop system input corresponds to disturbances that are expected to act upon the system. The minimization of the closed loop H_2 norm is equivalent to the minimization of a quadratic cost function associated with the norm of the control input and performance output [41], [45]:

$$J = \int_0^\infty [\boldsymbol{z}^T \boldsymbol{W}_{zz} \boldsymbol{z} + \boldsymbol{u}^T \boldsymbol{W}_{uu} \boldsymbol{u}] dt \tag{26}$$

where $\boldsymbol{W}_{zz}$ and $\boldsymbol{W}_{uu}$ are weight matrices defining the relative importance of input and output components.

Best possible performance is strongly dependent on the type of output provided to the controller: The guideline is to select the quantities that permit to best "capture" the structural behavior. In the present application as initial approach the measured LE and TE acceleration in two sections on the wing (tip and middle) are used for the controller design. Finally, for the experimental validation in the wind tunnel, a downgraded solution based on just one accelerometer used as output has been tested. Instead of using the accelerometric signal directly for the control feedback, the signals are numerically integrated to get approximate velocities using a pseudo-integrator of the form

$$I(s) = \frac{s}{s^2 + 2\xi\omega_0 s + \omega_0^2} \tag{27}$$

where $\omega_0 = 2\pi f_0$, $f_0 = 0.1Hz$ and $\xi = 1$. The use of an approximate integrator instead of an exact one has the double effect of removing the integration drift and of avoiding the controller operation at low frequencies.

The goal of the controller was to minimize the local velocities and accelerations in the range *24-60 m/s* by inserting the wing tip accelerations and velocities in the performance vector of the cost function to be minimized by the control tuning algorithm. The controller, based on the quadratic cost function, is stabilizing by definition, and the insertion of velocities and accelerations into the cost function was made in order to enforce a higher damping of the wing modes.

The main challenge in the design of a flutter suppression controller using a SOF controller is that the gain design algorithm needs to be initialized with a stable system, for which the cost function is well adapted. This requires either starting with a stable system or already having a stabilizing controller to initialize the algorithm with. The challenge here is that the minimization of the cost function used in the static output control (SOF) formulation is a minimization of dynamic response that, unlike the LQR case, pole assignments cases, or other techniques that guarantee stability, may not distinguish between a stable and unstable systems. Viewing this from an intuitive perspective this technique

can make a stable system “more” stable by reducing its dynamic response but only if the optimization is initialized with a stable system, and even then, care must be taken to ensure that during the optimization the system does not “jump” into the unstable domain. The system for which a flutter suppression controller is required is clearly not stable, and therefore it is not always easy to have a first-guess stabilizing controller. In the present application an envelope expansion approach was used: The controller was first designed at a speed lower than the flutter speed. Then the flight speed was increased slightly, and the optimization was performed again using the controller obtained at the previous step as the starting point. The procedure was then repeated until the full speed range was covered, then obtaining a controller able to stabilize the system beyond the flutter speed.

No gain scheduling was implemented. This was done not only for working with a simple controller but also to study the robustness of the resulting design in the face of speed and other system uncertainties. The general Simulink scheme of the wind tunnel model implementation of the SOF controller is shown in Fig. 17. The controller was digitally implemented with a system working frequency equal to *1 kHz*.

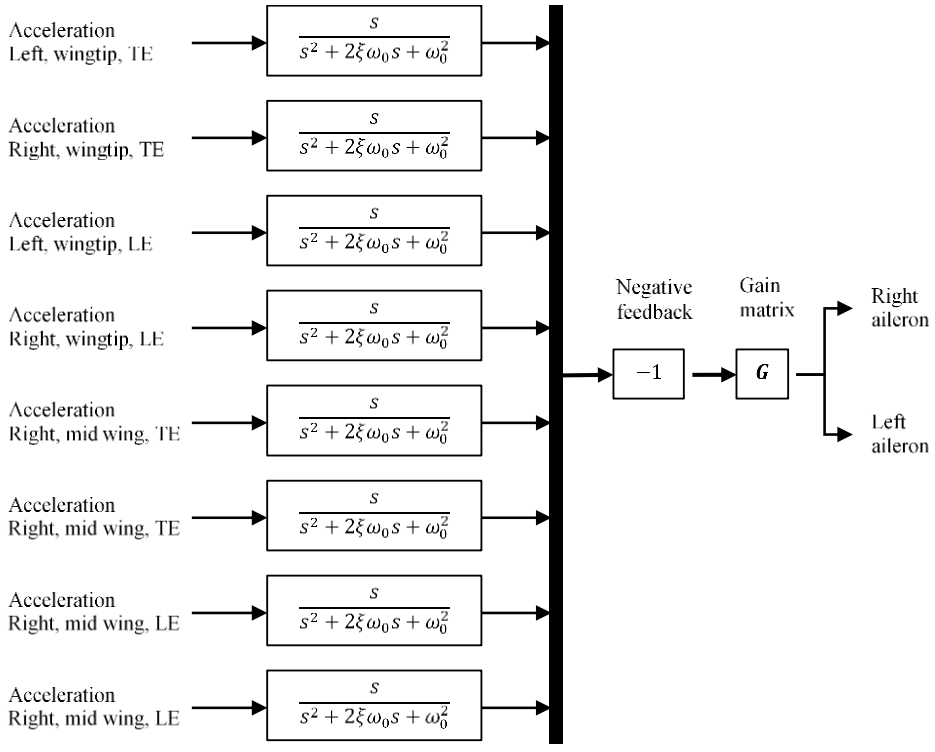

Fig. 17: SOF controller architecture.

VII. Numerical Aeroservoelastic Predictions

A. Numerical Flutter Identification in Open Loop

The FEM model of the aircraft, including a structural damping of *1%*, is used to perform a linear flutter analysis in NASTRAN (SOL 145). The results in terms of aeroelastic modal damping and frequency are presented in the velocity-frequency (*V-f*) and velocity-damping (*V-g*) plots of Fig. 18 and Fig. 19. This is for the model with it tip flutter stopper mass in the rear position. The flutter is predicted at an airspeed of $V_\infty = 40.7 m/s$ and the shape of the unstable mode is shown in Fig. 20: it is a coupling between the symmetric out-plane bending and the second torsion of the wing, the symmetric one, with a frequency of *6.35 Hz*.

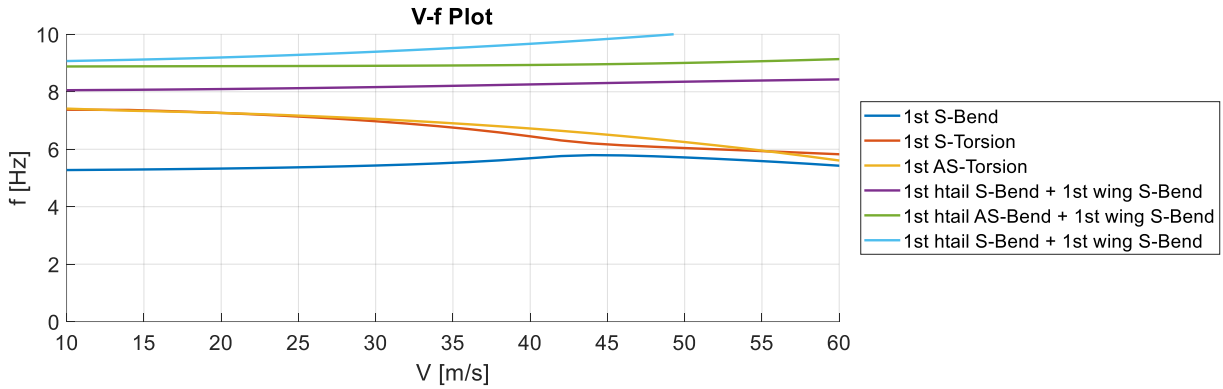

Fig. 18: Numerical V-f plot for the anti-flutter mass in rearward position

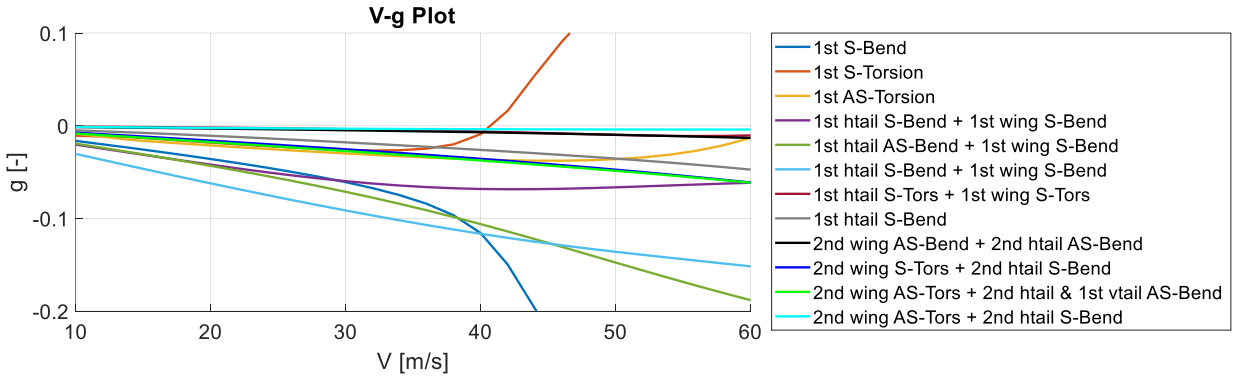

Fig. 19: Numerical V-g plot for the anti-flutter mass in rearward position.

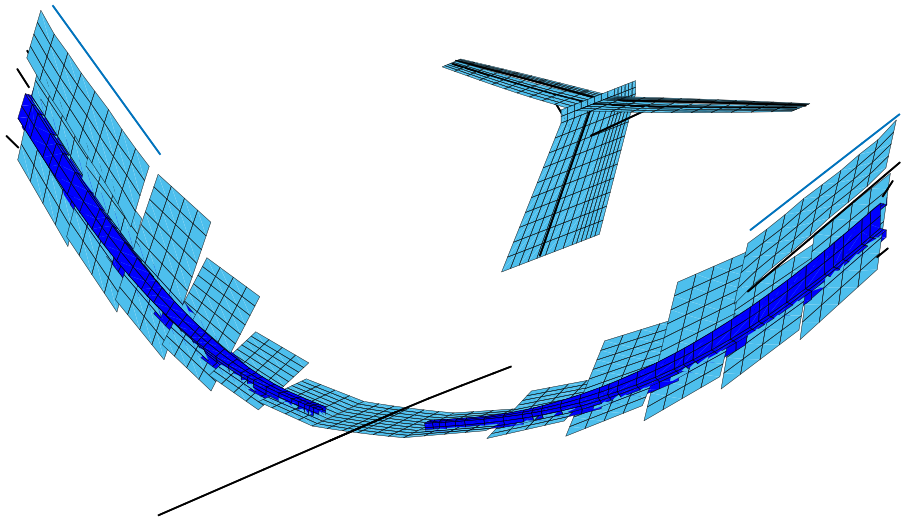

Fig. 20: flutter mode: coupling between 1st wing bending and 2nd wing torsion (symmetric).

B. Numerical Flutter Identification in Close Loop

In the implementation of the SOF designed for wind tunnel test validation described here, the integrated mean values of the two wing tips (LH and RH) leading edge accelerometers are used as outputs and the command input to the two ailerons is symmetric. This simplifies the structure of the gain matrix, which has a single parameter to be optimized as in Eq.(28):

$$G = \begin{bmatrix} g_1 & g_1 \\ g_1 & g_1 \end{bmatrix} \Rightarrow \begin{bmatrix} \delta_{LH} \\ \delta_{RH} \end{bmatrix} = 2g_1(\dot{x}_{LH} + \dot{x}_{RH}) \tag{28}$$

As in the ILAF approach, the SOF controller here provides a force input, through the aileron deflection, that is proportional to the wing tip out of plane velocity and is comparable to a viscous damping. It is emphasized again, that just selected results with a simple controller are presented here using a system that allows the testing of many alternative flutter suppression laws.

Fig. 21 shows the evolution of the poles of the aero-servo-elastic numerical system, increasing the gain value from 0 to 1 with 0.01 steps. Without a weighting function, the gain optimization would lead to a solution close to the stability margin with $g_1 = 0.85$. A weight function on the damping of the aeroelastic mode that becomes unstable for $g_1 > 0.85$ provides an optimized gain value of $g_1 = 0.25$. With this latest gain matrix, the poles of the closed loop aero-servo-elastic system are the ones in Fig. 22, where the system is stabilized and damping of the critical mode is maximized.

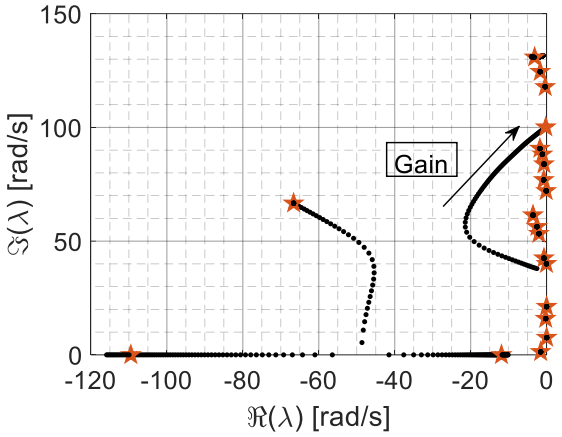

Fig. 21: Poles evolution at 45 m/s increasing g_1 up to the stability limit

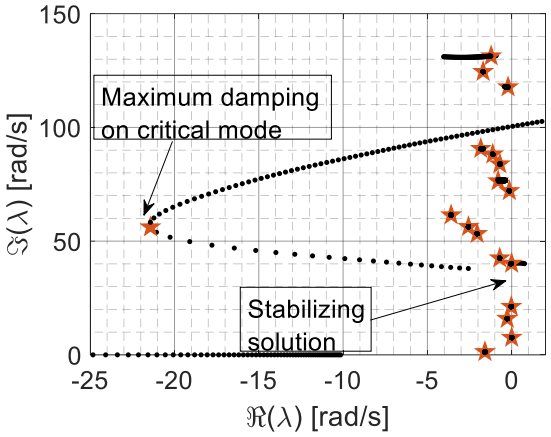

Fig. 22: Poles for the optimized gain $g_1 = 0.25$, zoom on real axis

Fig. 23 compares the open and closed loop root loci with the optimized SOF gain matrix, increasing the airspeed (bigger marker indicates 10m/s multiples). The flutter point of the closed loop system is moved to a value between *46* and *47m/s* and it is reached with a gentler $\frac{\delta\xi}{\delta V_\infty}$ ratio with respect to the open loop values. The open loop equivalent pole at *46 m/s* is highlighted by a circle and indicates where the pole would be without the AFS law.

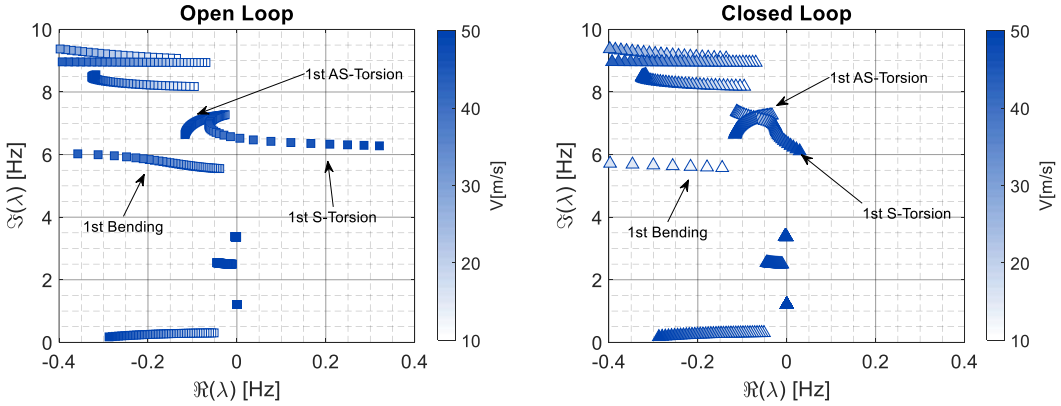

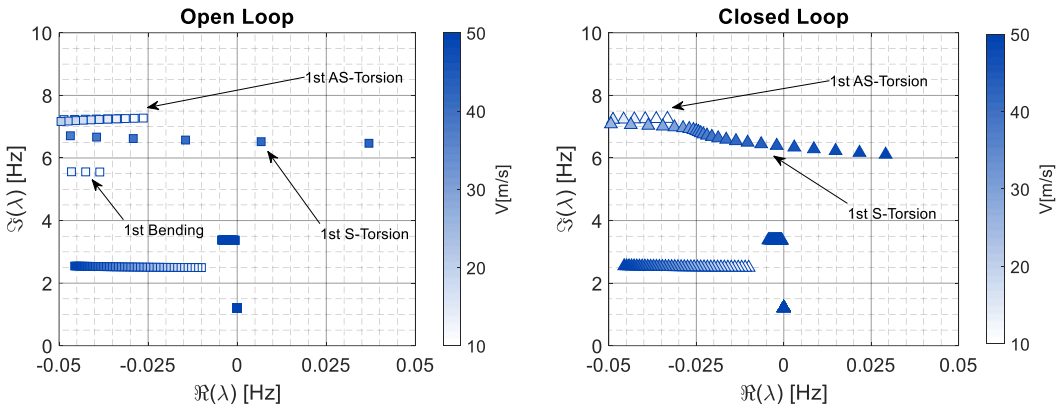

Fig. 23: Comparison of the open (left) and closed loop root loci (right). Bottom diagrams are the zoomed versions of previous ones.

VIII. The Wind Tunnel Tests

To structure the wind tunnel test campaign in a way that would best support the development of the new wind tunnel model system, in an effort to decrease the complexity of the tests due to the many parameters and potential uncertainties involved, the wind tunnel campaign was divided into two phases: In PHASE I the half wing, in clamped configuration, was tested for perfecting the identification of the flutter velocity and to set up and test the sensors and data acquisition system as well the controllers. In PHASE II the wind tunnel test on the complete model was carried out aiming at active flutter suppression validation and active control robustness checks.

PHASE I was carried out in the POLIMI Department of Aerospace Science and Technology's small Wind Tunnel, equipped with a test chamber of *1.5x1x3m* and a maximum velocity of *55 m/s*. Then, the full F-XDIA model was tested in a free-free configuration in the POLIMI's large wind tunnel. This tunnel is based on an unconventional configuration, i.e. a closed circuit where the return circuit is used for wind engineering tests with a large testing room sized *4x14x34m*. Two moving test chambers for aerospace testing are available, sized 4x4x6m with a maximum speed of *55m/s*. Despite the low Mach number, the large size of the chamber allows testing of large-scale models. The results of the PHASE I experimental campaign are reported in [22, 23]. The PHASE II experimental campaign focused on active flutter suppression systems validation and was carried out in 2020. It is described in detail in the following sections.

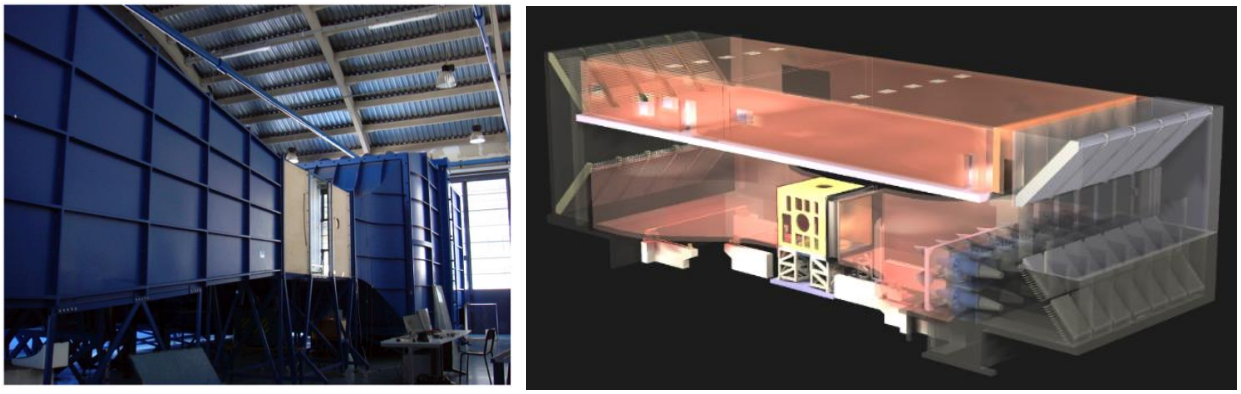

Fig. 24: The Department Wind Tunnel (left) and the POLIMI's Large Wind Tunnel (right).

While the PHASE I wind tunnel test was dedicated to the validation of the hardware and its improvement, the PHASE II tests were the most important in terms of final results. In particular, the first session, carried out in July 2019, allowed validation of the complete setup and identification of the flutter point, while the second session, carried out in January 2020, was dedicated to the validation of the three active flutter controllers listed above together with a first study (using the new system) of aeroelastic flutter suppression robustness by tests.

A. Model setup and experimental flutter identification

The wind tunnel flutter test campaign of the complete F-XDIA model was carried out in the large POLIMI's Wind Tunnel that is equipped with two interchangeable test chambers. One of them was equipped with the necessary hardware to suspend the F-XDIA model during the test. The adopted suspension system allows for a quasi-free-free configuration. The model was suspended by the fuselage with two steel cables connected to the roof of the chamber. Four additional nylon cables (two in the front and two in the rear part of the model) were connected to the vertical wall for safety, keeping the model in the middle of the chamber (see Fig. 25). Based on the mathematical predictions, the expected flutter mainly involved the wing with some contribution from the tail planes. The adopted suspension system, therefore, despite not being completely free-free, had a minimum impact on the flutter behavior.

The power systems for the electric drivers controlling the ailerons and the elevators as well the internet cable were running in a single umbilical cord along the front suspension cable. The test session was remotely managed from the wind tunnel control room. In this setup the operator, using a standard computer, can log in on to the on-board computer to start the test session, to work with the controller, and to manage the data acquisition system. The model is equipped

with 20 MEMS mono axial accelerometers plus one capacitive triaxial accelerometer located at the CoG. The aileron rotations are measured by means of the embedded encoders. Two linear actuators are used to statically trim the elevator. No automatic flight control system was implemented.

Four kinds of excitations were available during the wind tunnel test, applied using the model's ailerons: sine sweep excitation, impulse, white noise, and square wave.

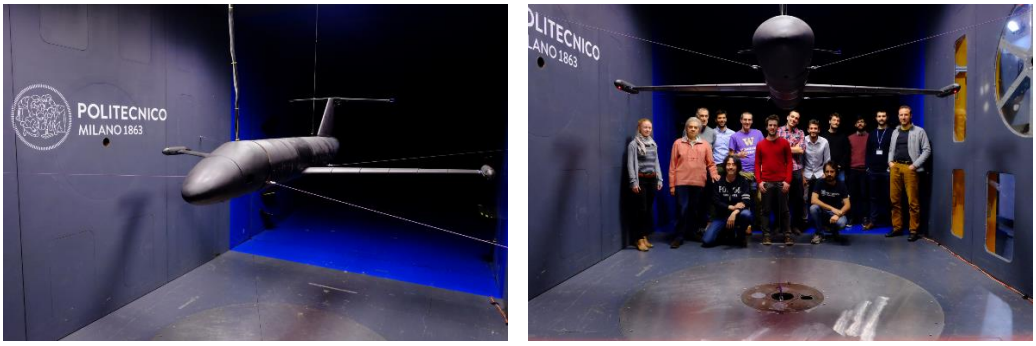

Fig. 25: The test setup inside the large POLIMI's wind tunnel. (Note: The presence of the people in the photo on the right gives a perspective of the size of the model)

B. Experimental Flutter Identification in Open Loop

The initial part of the final flutter test campaign aimed at the identification of the flutter behavior in the open loop configuration. For safety reasons, the first condition investigated was the one with the movable masses of the flutter-stopper system in the forward position (anti-flutter on position). The wind tunnel velocity was increased from $V_\infty = 0m/s$ to $V_\infty = 40m/s$ with $\Delta V_\infty = 5m/s$, above 40m/s the velocity step was decreased to *1m/s*. The model was excited with symmetrical and anti-symmetrical ailerons sweep with a frequency content between *4-9 Hz* and a duration of 50s (*45 s* of excitation and *5s* of stand-by between two sweeps), repeated 3 times. The frequency content and the time history of the sweep are shown in Fig. 26 and Fig. 27, with Fig. 27 representing the Fourier transformation of the measured aileron rotation.

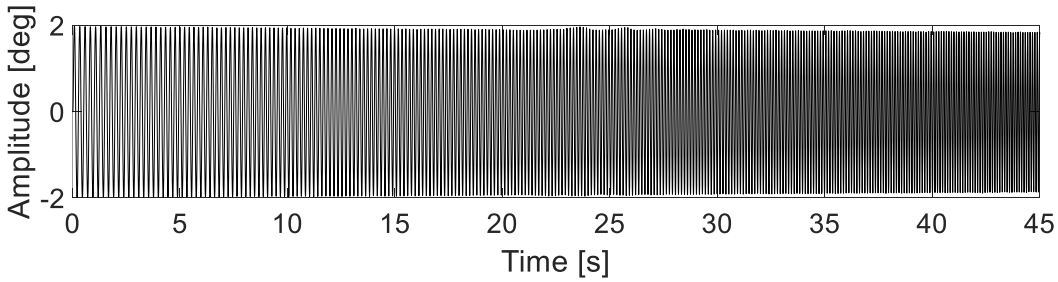

Fig. 26: Aileron rotation measured.

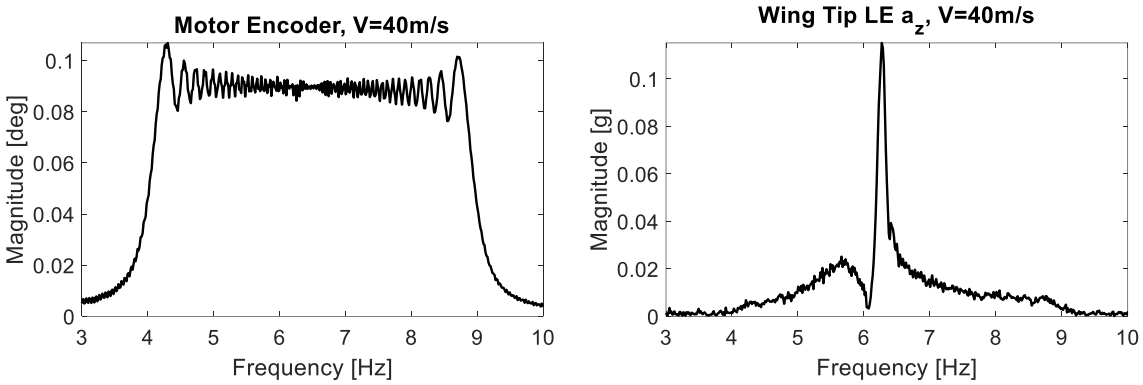

Fig. 27: Fourier's transformation of the aileron rotation excited with the sweep signal (left) and FRF of Left Wing LE tip vertical acceleration due to sweep excitation (right).

The experimental results were processed using two different algorithms for better results reliability: the ARX method implemented in Matlab [46] and using the Polymax method as implemented in SIEMENS-TestLab software [47]. Both methods use the complete data set of averaged FrFs to perform the identification. The results and the comparison with the numerical model are presented in Fig. 28 and Fig. 29, showing a good accordance between numerical and experimental values for the first three wing modes. The bold lines represent the NASTRAN's result while the markers represent the identified frequency and damping.

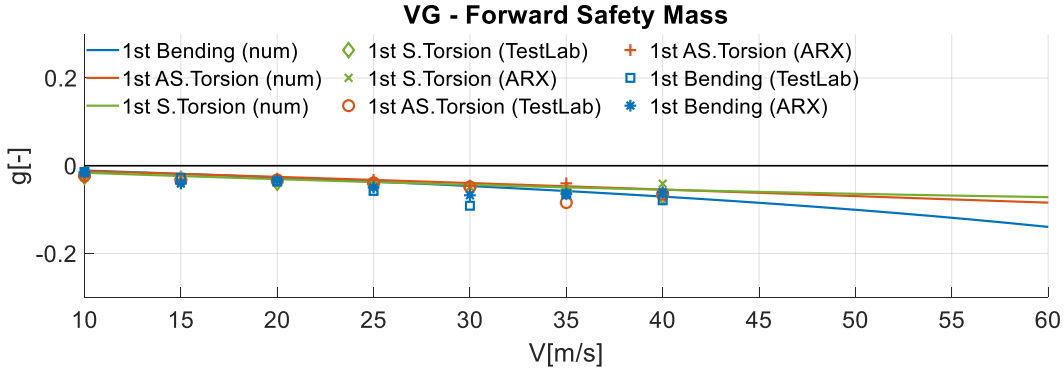

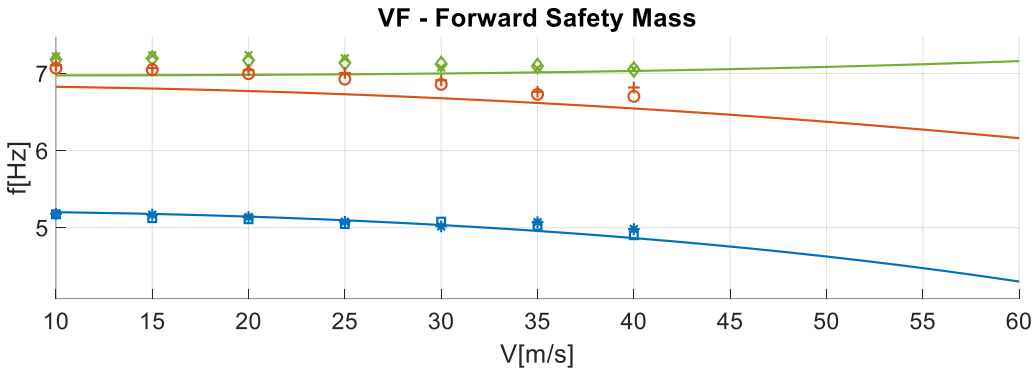

Fig. 28: V-f and V-g plot comparison, numerical vs. identified poles with different algorithms for the tip safety mass in the forward position

Once it was confirmed that the model with the flutter-stopper masses in safety position was stable across the entire flight envelope, it was possible to start the flutter investigation for the configuration with the masses in the rearward position (anti flutter effect off). In the case of flutter onset, the masses are automatically moved instantly to the forward position and the stability is recovered. Once the velocity of $V_\infty = 40m/s$ was reached, the velocity was slowly increased with *0.5m/s* steps and the model was excited with an impulse with increasing amplitude to gently approach the flutter point, which was identified at $V_{flutter} = 41.5\ m/s$. As in the previous case, the results were processed to identify frequency and damping of the first 3 wing's mode poles with the algorithms listed above. The experimental results are reported in Table 6 and Table 7 and they are compared with the numerical simulation in Fig. 29, showing a good correlation once again.

Table 6. Open Loop Experimentally Identified Frequencies.

	ARX [Hz]			PolyMax [Hz]		
V [m/s]	**Bending**	**Asim-Torsion**	**Sim-Torsion**	**Bending**	**Asim-Torsion**	**Sim-Torsion**
0	5.24	7.33	7.41	5.21	7.33	7.38
10.0	5.26	7.44	7.44	5.23	7.32	7.37
15.0	5.30	7.32	7.24	5.26	7.30	7.35
20.0	5.32	7.26	7.19	5.28	7.25	7.28
25.0	5.35	7.17	6.99	5.32	7.14	7.11
30.0	5.64	7.05	6.69	5.43	7.00	6.93
35.0	5.56	6.84	6.73	5.53	6.83	6.67
37.5	5.65	6.79	6.58	5.61	6.72	6.51
40.0	5.97	6.65	6.33	5.73	6.62	6.30

Table 7. Open Loop Experimentally Identified Damping Factors.

	ARX [%]			PolyMax [%]		
V [m/s]	**Bending**	**Asim-Torsion**	**Sim-Torsion**	**Bending**	**Asim-Torsion**	**Sim-Torsion**
0	-1.88	-0.02	-0.02	-0.01	-1.44	-0.02
10.0	-2.76	-2.36	-2.96	-2.00	-2.16	-2.04
15.0	-3.44	-3.78	-4.00	-3.04	-2.84	-2.52
20.0	-4.58	-2.92	-4.02	-4.04	-3.06	-2.96
25.0	-5.06	-3.64	-3.56	-6.64	-3.36	-3.40
30.0	-6.46	-4.16	-3.68	-7.40	-3.90	-3.62
35.0	-6.46	-4.10	-3.60	-8.08	-4.22	-3.56
37.5	-7.86	-5.42	-3.30	-9.34	-4.66	-3.30
40.0	-9.30	-4.58	-2.34	-10.06	-4.94	-1.88

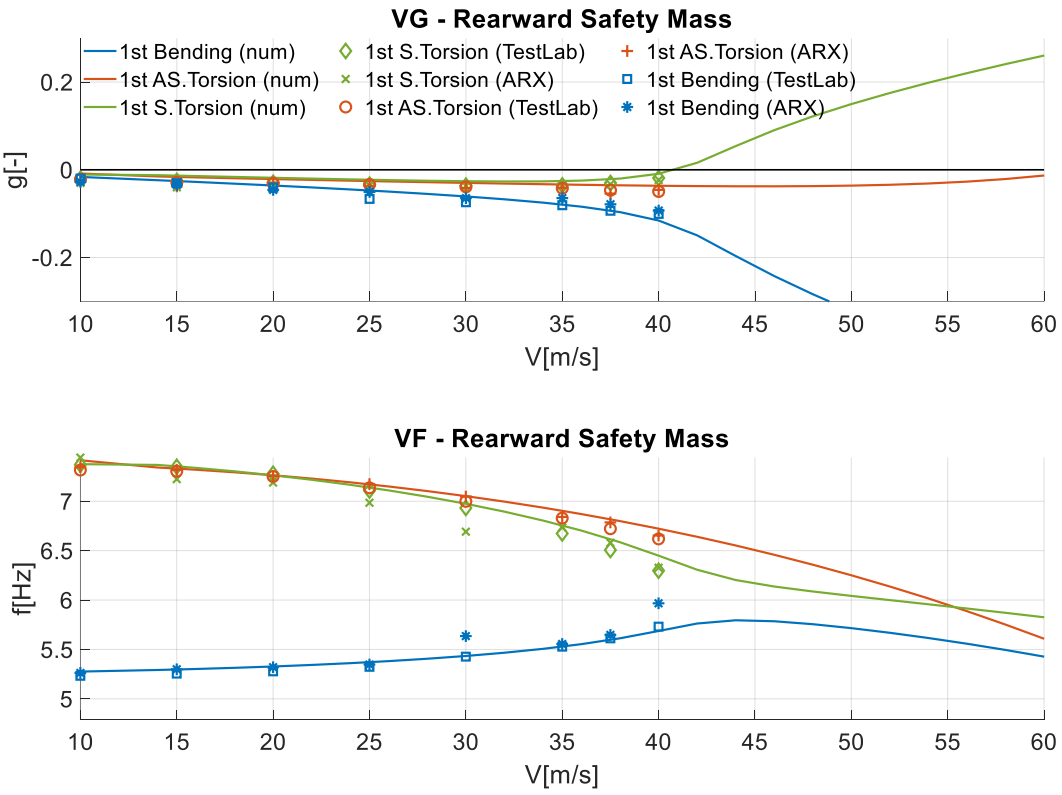

Fig. 29: V-f and V-g plot comparison, numerical vs. identified with the different ID algorithms for the tip safety mass in rear position

The experimental results presented so far show that the numerical model "captures" the experiment well: the frequency and damping values of the modes are similar in the two cases. The experiment confirms the interaction of the symmetrical torsion flutter mode with the bending one, as the coalescence of the frequencies suggest. The quality

of the experimental poles characteristics is confirmed by the consistency of the results obtained with two different methodologies, leading in the cases described here to low-scatter in the results.

During this identification phase, the flutter stopper device was tuned as well to establish a threshold on the wing tip acceleration that would automatically activate the safety system. The threshold was set to a value of $a_{MAX} = 4g$ for the wing tip's LE accelerometers. The tuning of the safety device proved to be very useful during the test campaign, where the flutter point was reached many times and with different type of excitation.

To better support on-line flutter poles analyses using a recursive Extended-Least-Squares/Maximum-Likelihood multi-input single-output real time identification [48], pseudo white noise control surface commands were used. Such a forcing function provides an excitation band matching the actuator's and allows an a posteriori cross verification on the basis of the processing of offline data using standard frequency response methods.

Fig. 30 shows the case where the model was tested with a white noise input at the flutter velocity exactly. Looking at the acceleration measured on the left-wing tip, it is possible to recognize an initial phase where the response is purely random, then a transition phase begins, and finally the steady harmonic oscillation starts with increasing amplitude until the intervention of the flutter stopper system that moves the tip mass to the forward position to stop the flutter oscillation.

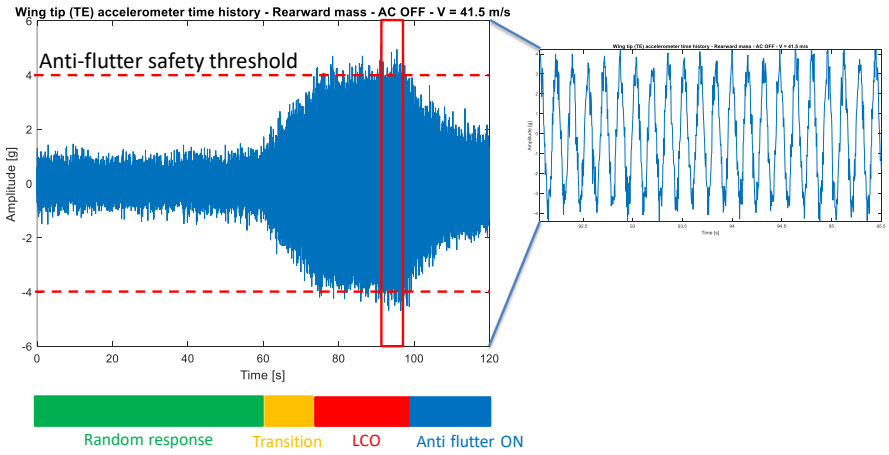

Fig. 30: Measured response (tip acceleration) @ flutter speed, 41.5 m/s.

C. Experimental Flutter Identification in Closed Loop Case

The designed static output feedback (SOF) controller described above was tested to identify the closed-loop flutter point, where the wind tunnel model is "flown" beyond its open loop flutter point. On the basis on the knowledge acquired during the open loop test case, the testing strategy was slightly changed. First, from 0 to 40 m/s the previously described aileron sweep excitation was applied at *20*, *30* and *40 m/s*. The model was excited with a symmetrical aileron frequency sweep described by Eq.**(**29**)**, with the lowest frequency $f_0 = 4\ Hz$, maximum frequency $f_1 = 9Hz$ and a duration $T = 50s$.

$$\delta(t) = \delta_A \sin\left(2\pi\left(f_0 + \frac{f_1 - f_0}{T}t\right)t\right) \tag{29}$$

The model was excited up to $V_\infty = 40m/s$ both in open and closed loop configuration and the data acquired was processed with the ARX algorithm presented in [46], which provides the Frequency Response Functions between the aileron rotation inputs measured with the encoders and the output acceleration. Fig. 31 shows the evolution of the FrF sum with the increasing airspeed with and without the active control. Without active control the bending mode frequency increases with the dynamic pressure while the torsional mode frequency decreases. At $V_\infty = 40m/s$ the frequency separation between the two modes is small and a slight increase in the airflow speed, i.e. *1.5m/s*, leads to the coalescence of the two modes that is associated with coupled bending-torsion flutter

The SOF controller acts by adding damping, and the peak related to the aeroelastic modes are lower in magnitude while the peak related to the instability mode at $V_\infty = 40m/s$ is flattened. The FrF sum for $V_\infty = 40m/s$ is shown in Fig. 32. Fig. 33 shows the comparison between the open and closed loop wing tip acceleration due to a frequency sweep input when the signals are filtered at *100Hz* to remove the noise and the frequency content one order of magnitude higher than the bandwidth of interest *0-10Hz*. The x axis shows both time and the frequency of excitation at that time. The lower axis shows the time and the upper indicates the input frequency, generated by the relation in Eq.(29). When the excitation reaches the frequency of the torsional mode (*6.0-6.4Hz*), the amplitude of the acceleration increases in open loop, while the controlled model amplitude is almost constant over the same frequency range.

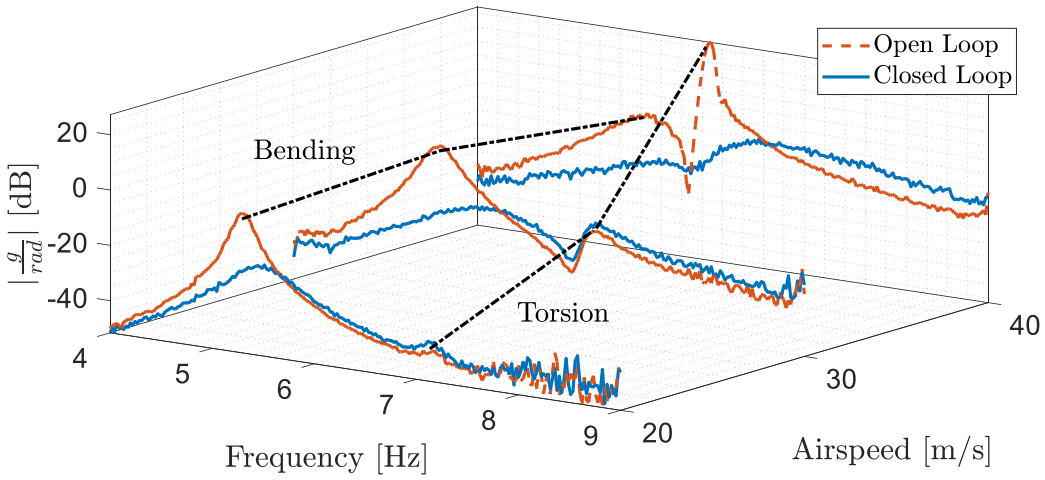

Fig. 31: Open and closed loop Frfs sum evolution with the airspeed.

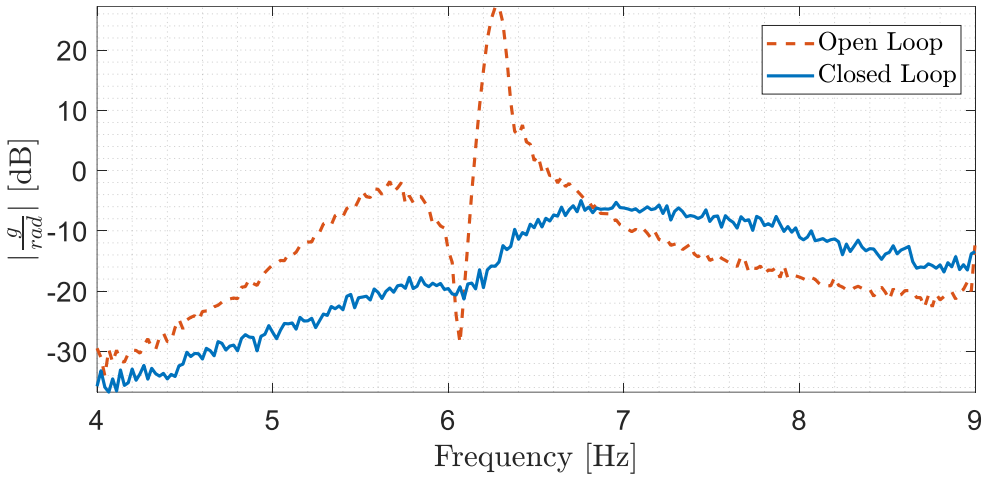

Fig. 32: Comparison between open and closed loop Frfs sum at 40m/s

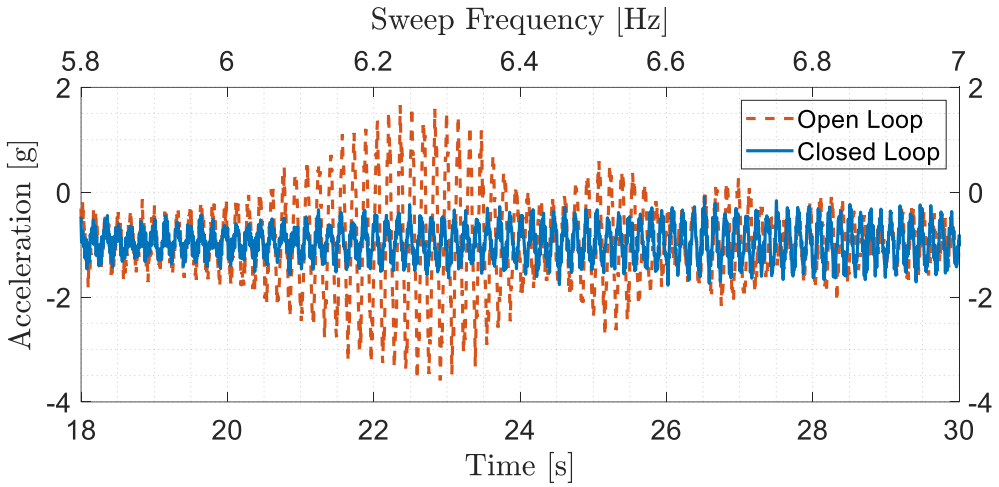

Fig. 33: Open and closed loop wing tip acceleration at V=40 m/sec due to the sweep input excitation, with the signals filtered at 100Hz

The experimental results presented so far were obtained below the Open Loop flutter velocity and for such airspeeds it is possible to compare the results obtained both in Open and Closed Loop. For airspeeds above $V_\infty = 41.5 m/s$ there are no results for the Open Loop configuration due to the flutter onset.

The excitation signal above $V_\infty > 41.5\, m/s$ was changed into the white noise, which was already introduced during the open loop tests, with prescribed amplitude and used as input for moving the control surfaces. The change in the excitation method was made since frequency sweep excitation was found to be too aggressive at speeds above the open-loop flutter speed even with limited amplitudes of $\delta = 1 deg$. When the flutter appeared, the flutter-stopper devices worked perfectly by stopping the flutter very quickly without the need to decrease the wind tunnel velocity, as shown in Fig. 30.

Table 8 presents the evolution of the flutter poles in term of frequency and damping for both the experimental data and the numerical results. The experimental data were used to compute the transfer function between the aileron rotation input and the wing tip leading edge accelerometer. The flutter mode frequency and damping were identified using the algorithms used for open loop identification, i.e. ARX [46] and Polymax [47]. The ARX algorithm tries to fit in the least-square sense the estimated FRF with a number of poles indicated by the user. The order of the rational polynomial formula is the result to the attempt to fit as best as possible the peaks in terms of frequency, amplitude, and width. Following this criteria, the order shows this tendency: The lower the velocity is the higher is the order required, considering obviously a velocity range around the flutter point (from *41.5* to *45.5 m/s*). This is due to the

interaction of two modes: When the velocity is far away from the flutter condition the modes coalescence has not been fully completed yet, so they are distinct enough and the algorithm needs more poles to follows these abrupt changes in a such a narrow band. When the flutter effects becomes important, the controller start to restrict the structural response producing only one distinguishable peak, which is easier to capture by the identification fitting process. Generally the number of poles used goes from 50 to 150.

Table 8: Flutter mode evolution for the controlled system

	ARX		Polymax		Numerical	
V [m/s]	f [Hz]	ξ [%]	f [Hz]	ξ [%]	f [Hz]	ξ [%]
40.50	6.45	2.75	6.40	1.39	-	-
41.00	6.22	4.95	6.25	1.42	6.49	1.31
41.50	6.45	5.27	6.23	1.86	-	-
42.00	6.23	4.85	6.27	2.33	6.43	1.29
42.50	6.23	3.66	6.19	1.41	-	-
43.00	6.50	4.78	6.41	2.78	6.36	1.25
43.50	6.31	4.63	6.35	2.71	-	-
44.00	6.40	4.48	6.26	3.30	6.30	1.20

In general, the identification methods used overestimated the damping of the pole and underestimated its frequency. This can be seen in Fig. 34, where the ARX identification methods does not properly identify the presence of two peaks, with a little shift in the frequency peaks and an overestimation of the peak amplitude. Fig. 35 shows the typical stabilization diagram during the identification performed by Polymax, showing the poles evolution with increasing the order of the system. The frequency shift is still present, but the pole's damping estimation is closer to the numerical results.

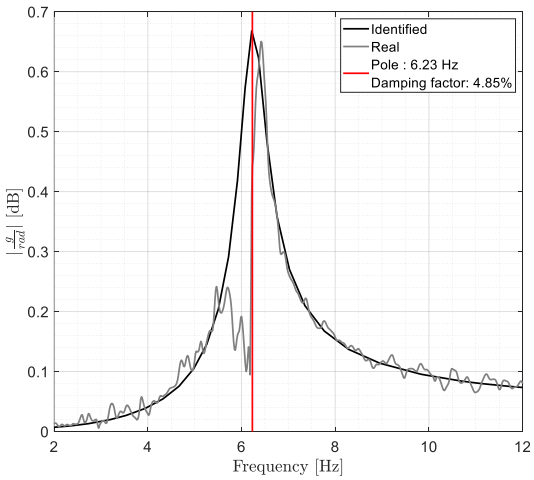

Fig. 34: ARX identification at 42m/s

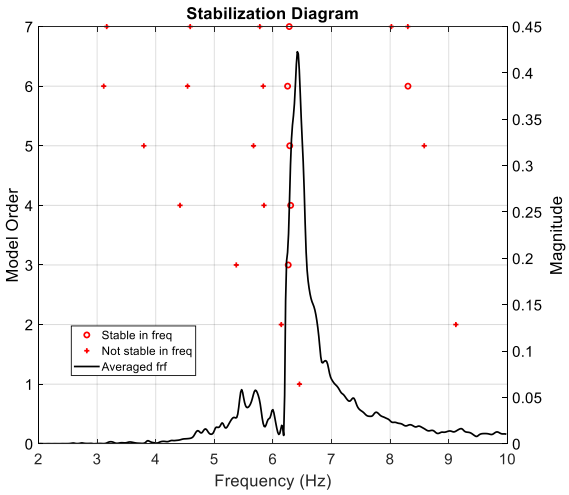

Fig. 35: Polymax identification at 42m/s

These results show that the SOF controller increases the system stability below the flutter point and it allowed opening of the flight envelope at higher wind tunnel speeds. The wind tunnel speed was increased up to the flutter point and beyond, where obviously it was impossible to collect data for the open loop case. The excitation beyond the flutter point was provided by a white noise signal with *10 degs* amplitude as explained earlier, aiming at a possible real time identification of flutter characteristics before the final post processing. The speed was increased at 1m/s steps reaching $V_\infty = 47m/s$ and still maintaining the stability of the system. Higher velocities were not investigated because the numerical results of Fig. 31 indicate $46 < V_\infty < 47m/s$ as closed-loop flutter onset and because of concerns about the effectiveness of the flutter stopper so far away from the open-loop flutter speed.

These tests showed that the control system with its nominal design gains efficiently suppressed the flutter and moved the flutter boundary above $V_\infty = 47m/s$, which is equivalent to about 28% increase in the dynamic pressure.

D. Robustness checks

Once the efficiency of the SOF controller was verified, it was possible to proceed to tests of the robustness of the closed loop system. A certain measure of control system robustness was demonstrated by using a single gain in the SOF law, without any gain scheduling, to cover a rather large range of dynamic pressures below and above the open-loop flutter condition well. The tests of system robustness described next focused on the robustness of the system to changes in gains and delays in the control system, which simulate actual changes of gains and delay in the control

system, or changes in input-output gains and phase in the actual characteristics of the aeroservoelastic model compared to the mathematical model used to synthesize the control laws, or both, as represented in Fig. 36.

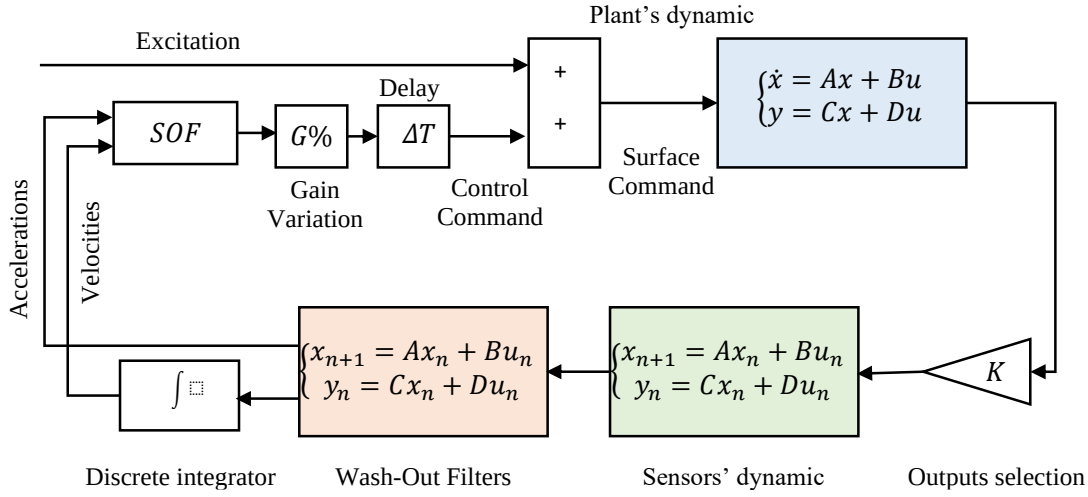

Fig. 36: Simulink scheme with blocks for gain variation and input delay

For the first test, the nominal gains of the SOF gain matrix were changed over a range of 20%-200%, while testing the aircraft at the open-loop flutter point. Over this range of gains variations, the system remained stable at the flutter point, i.e. $V_\infty = 41.5 m/s$. Fig. 37 shows as an example the time histories of wing tip acceleration corresponding to Gain equal to 0.2, 0.4 and 1.0, respectively.

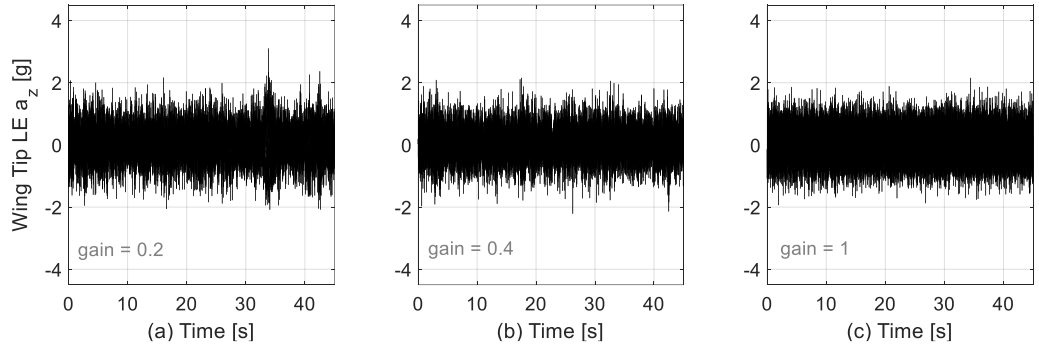

Fig. 37: Time histories of wingtip Z acceleration at *V=41.5 m/s* for Gain equal to *0.2* (a), *0.4* (b) and *1.0* (c), respectively.

Then, for the same values of Gain the wind tunnel flow velocity was increased to *46* and to *50 m/s* without any flutter phenomenon, as reported in Fig. 38 corresponding to *V=50 m/s*.

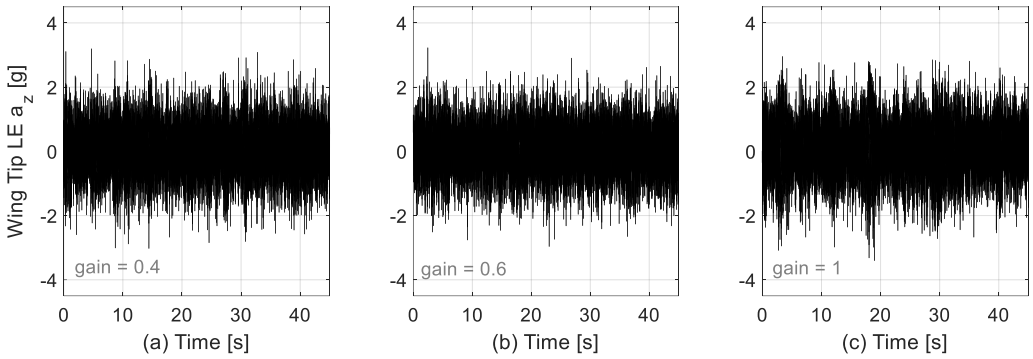

Fig. 38: Time histories of wingtip Z acceleration at *V=50 m/s* for Gain equal to *0.2* (a), *0.4* (b) and *1.0* (c), respectively.

The second test of control robustness was performed by adding an artificial delay to the control command. At the flutter point the aircraft was stable even with a delay of 10ms. To "challenge" the controller, a test with 5ms delay and nominal gains was performed at $V_\infty = 45 m/s$ (quite above the open loop flutter speed) and the model was still stable. Table 9 provides a summary of the SOF robustness investigations carried out during the tests in the large POLIMI wind tunnel. A more detailed robustness analysis of SOF controller together with the other controllers tested during the wind tunnel experimental campaign, and not reported here, can be found in [40].

Table 9: SOF robustness tests summary table

$V_\infty [m/s]$	Gain [%]	Delay [ms]
0-47	100	0
41.5-50.0	20-200	0
41.5	100	10
45	100	5

In conclusion, the designed SOF controller was able to control the flutter instability and to expand the flight envelope by 13% in terms of airspeed (about 28% in dynamic pressure). The simple design methodology proved to be robust with respect to gain variation and delays as well as dynamic pressures. The design choice of using a mean value of the wing tip velocity together with the stability of the system with 50% of the nominal gains ensures the flutter control even in case of loss of one of the two accelerometer, demonstrating a natural redundancy of the controller.

IX. Conclusions

The paper describes the full development for active flutter suppression research of a wind tunnel system with a large size aeroservoelastic wind tunnel model of a representative jet transport at its center. Description of tests used to validate mathematical models and then an active flutter suppression control law is also included to provide information that other researchers working in this area and developing their own active flutter suppression laws will be able to benefit from.

The development process included two phases: the first one based on a half wing only in a small wind tunnel, and the second one focused on the complete model. Phase I (not described in detail here but covered in earlier papers) allowed validation of the general approach, the hardware and software for the wind tunnel test campaign, as well the capability to control the flutter instability. In Phase II (the main focus of this paper) the entire model with all supporting hardware was completed, including the onboard computer and systems. The thorough test campaign in the large wind tunnel provided a full validation of the systems involved.

A significant part of the work was dedicated to the structural dynamic modeling aspects of the F-XDIA model. A hybrid model of the structure made of a combination of stick model parts and detailed fine-mesh plate and solid element parts was found to be the best compromise between accuracy and computational effort. Detailed modeling of the wing was required due to the particular omega shape shape of the cross section. Shell elements were used for the wing-spar and solid elements for the wing / fueslage clamp to capture the wing torsional behavior well as well as the local flexibility of the wing root asttachements.

Similarly, the structural dynamic influence of the flutter stoppers had to be modeled carefully, including the effect of the location of the moving mass and the way the flutter stopper was attached to the wing tip. The structural dynamic modelling improvements were confirmed by the GVT's results.

From an unsteady aerodynamics modeling perspective, the inclusion of the tip flutter-stopper bodies was found to be quite important. In an effort to work with a computationally efficient structural dynamic model, the wing-tip flutter stoppers wee modeled using slender bodies, but to account for their not-so-slender shape and the presence of slots between them and the wing, they were modelled as less effective by a certain percentage than what their ideal geometry would lead to. The resulting NASTRAN / DLM based model of the wind tunnel model was found to predict the aeroelastic behavior of the model well, including the behavior with flutter-stopper masses in the forward and rear positions, the flutter mechanisms, and the open-loop flutter speed.

On the basis of the aeroservoelastic math model describing the F-XDIA model different Active Flutter Suppression controllers were developed. The synthesis of an SOF controller and closed-loop test results with it were described in this paper.

The wind tunnel tests in the large wind tunnel with the full wind tunnel model, after studying the open loop behavior of the system, focused on the flutter suppression capabilities of the controllers and their robustness. Two kind of uncertainties were introduced during the experimental campaign: a scaling of the reference gains as well pre-defined delays inserted into the control loop. These changed the dynamics of the system to be controlled by the nominal control law without the need to stop the tests for actual mass and stiffness (or aerodynamic) changes that would then be tested with the nominal control law. This approach, it should be noted, can simulate more uncertainties in the structural and aerodynamic characteristics of the system when multi-input multi-output (MIMO) controllers will be tested. Additional wind tunnel runs were carried out with combinations of uncertainties using asymmetric excitations to better understand the behavior of the model. All the proposed controllers worked well, with slightly different performance in terms of increased flutter speed. Differences have been found in terms of robustness. This will be reported in follow on publications.

The new system developed, including hardware and software, was found to be very efficient and highly reliable. In particular, the flutter stoppers made it possible to reach the exact flutter point many times without damaging the model or switching off the wind tunnel. This allowed testing at many flutter conditions during the same test run.
The large amount of measured data opens the path for further investigations to improve the simulation models as well as to better identify the most promising flutter control technologies. The model, the system, and the data will be available for research development in the active flutter suppression area by others.

Acknowledgements

Support by the Federal Aviation Administration as well as contributions by Wael Nour and Sohrob Mottaghi from the FAA are gratefully appreciated. A special thanks to graduate students Francesco Lo Balbo and Domenico Di Leone for their support during the Wind Tunnel tests and for the post processing activity. The continued support of Giampiero Bindolino is highly appreciated.

References

1. Livne, E., "Aircraft Active Flutter Suppression: State of the Art and Technology Maturation Needs", *Journal of Aircraft*, Vol. 55, No. 1, Jan.-Feb. 2018, pp. 410-452, doi: 10.2514/1.C034442

2. Bisplinghoff, R.L., Ashley, H., and Halfman, R.L., Aeroelasticity, Addison-Wesley Publishing Company 1955 (available in a Dover Publications edition), Chapters 12-13.

3. Dupriez, F., "Flutter Models – Their Design, Manufacture, and Ground Testing", in "Introduction to Flutter of Winged Aircraft", von Karman Institute for Fluid Dynamics, Lecture Series 1992-01, December 1991.

Busan, R., "Flutter Model Technology", US Air Force Wright Laboratory, WL-TR-97-3074, January 1998 (also, section 7 in NASA Aeroelasticity Handbook, Volume 2: Design Guides, Part 2, NASA/TP-2006-212490/VOL2/PART2, John K. Ramsey, editor,

https://ntrs.nasa.gov/api/citations/20070008370/downloads/20070008370.pdf

4. Wasserman, L.S., "Flutter Model Design and Ground Vibration Testing", Section 2 in NASA Aeroelasticity Handbook, Volume 2: Design Guides, Part 2, NASA/TP-2006-212490/VOL2/PART2, John K. Ramsey, editor, https://ntrs.nasa.gov/api/citations/20070008370/downloads/20070008370.pdf

5. Redd, L.T., Gilman, Jr., J., Cooley, D.E., and Sevart, F.D., "Wind-Tunnel Investigation of a B-52 Model Flutter Suppression System", *Journal of Aircraft*, 1974, Volume 11, No. 11, pp. 659-663, doi: 10.2514/3.60401

6. Sevart, F.D., "Development of Active Flutter Suppression Wind Tunnel Testing Techno,logy", AFFDL Report AFFDL-TR-74-126, January 1975, AD B 002840, https://apps.dtic.mil/dtic/tr/fulltext/u2/b002840.pdf

7. Peloubet, R.P., Jr., Haller, R.L., and Bolding, R.M/. "F-16 Flutter Suppression System Investigation Feasibility Study and Wind Tunnel Tests", *Journal of Aircraft*, 1982, pp. 169-175, Vol. 19, No. 2, doi: 10.2514/3.57371

8. Hwang, C., Johnson, E.H., and Pi, W.S., "Recent Development of the YF-17 Active Flutter Suppression System", *Journal of Aircraft*, Vol. 18, No.7, 1981, pp. 537-545, doi: 10.2514/3.57523

9. French, M., and Kolonay, R.M., "Demonstration of Structural Optimization Applied to Wind Tunnel Model Design", *Journal of Aircraft*, 1991, Vol. 29, No. 5., pp. 966-968, doi: 10.2514/3.46271

10. Britt, R., Ortega, D., Mc Tigue, J, and Scott, M., “Wind Tunnel Test of a Very Flexible Aircraft Wing”, AIAA Paper 2012-1464, doi: 10.2514/6.2012-1464

11. Pankonien, A.M., and Reich, G.W., “Multi-Material Printed Wind-Tunnel Flutter Model”, *AIAA Journal*, 2017, Volume 56, Issue 2, doi: 10.2514/1.J056097

12. Burnett, E.L., Beranek, J.A., Holm-Hansen, B.T., Atkinson, C.J., Flick, P.M., 2016, “Design and flight test of active flutter suppression on the X-56A multi-utility technology test-bed aircraft”, *The Aeronautical Journal*, 120:1228, pp. 893-909.

13. Regan, C.D., and Taylor, B.R., “mAEWing1: Design, Build, Test”, AIAA Paper 2016-1747, doi: 10.2514/6.2016-1747

14. Regan, C.D., “mAEWing2: Conceptual Design and System Test”, AIAA Paper 2017-1391, doi: 10.2514/6.2017-1391

15. Precup N., Mundt, T., Mor, M., and Livne, E., “An Active Variable Camber Continuous Trailing Edge Flapped Wing Wind Tunnel Model for Aeroelastic ‘‘In-Flight Shape Optimization Tests”, AIAA Paper 2018-3106, AIAA Aviation 2018 Forum, Atlanta, GA, June 2018, doi: 10.2514/6.2018-3106

16. Regan, C.D., Kotikalpudi, A., Schmidt, D.K., and Seiler, P.J., “mAEWing2: Initial Flight Test and System Identification of a Flexible UAV”, AIAA Paper 2020-1965, doi: 6.2020-1965

17. Schmidt, D.K., Danowsky, B.P., Kotikalpudi, A., Theis, J., Regan, C.D., Seiler, P.J., and Kapania, R.K., ”Modeling, Design, and Flight Testing of Three Flutter Controllers for a Flying-Wing Drone”, *Journal of Aircraft*, 2020, Volume 57, Issue 4, doi: 10.2514/1.C035720

18. Stahl, P., Sendner, F-M, Hermanutz, A., Rößler, C., and Hornung, M., “Mission and Aircraft Design of FLEXOP Unmanned Flying Demonstrator to Test Flutter Suppression within Visual Line of Sight”, doi: 10.2514/6.2017-3766

19. Ricci, S., Scotti, A., Cecrdle, J., and Malecek, J., “Active Control of Three-Surface Aeroelastic Model”, *Journal of Aircraft*, 2008, Vol.45, pp. 1002-1013, doi: 10.2514/1.33303.

20. De Gaspari, A., Ricci, S., Riccobene, L., and Scotti, A.," Active Aeroelastic Control Over a Multisurface Wing: Modeling and Wind-Tunnel Testing", *AIAA Journal*, 2009, Vol.47, pp.1995-2010, doi: 10.2514/1.34649

21. Fonte, F., De Gaspari, A., Riccobene, L., Toffol, F., Malik, S., Marchetti, L., Ricci, S., Mantegazza, P., and Livne, E., "Development of a Wind Tunnel Model for Active Flutter Suppression Studies", AIAA Scitech 2019 Forum, 7-11 January 2019, San Diego, California, USA, doi: 10.2514/6.2019-2029

22. Marchetti, L., De Gaspari, A., Riccobene, L., Toffol, F., Fonte, F., Ricci, S., Mantegazza, P., Livne, E., and Hinson, K., "Active Flutter Suppression Analysis and Wind Tunnel Studies of a Commercial Transport Configuration", AIAA Scitech 2020 Forum, 6-10 January 2020, Orlando, FL, USA, doi: 10.2514/6.2020-1677

24. Martina, A.P., and Young, G.E., "Results of Initial Wind-Tunnel Flutter Experiments at Low Speeds with a Towed Airplane ModelHaving a 400 Sweptback Wing of Aspect Ratio 3.62 Equipped with Pylon-Mounted Stores", NACA Research Memorandum RM L54K17, March 24, 1955.

25. H. N. Murrow and C. V. Eckstrom, "Drones for Aerodynamic and Structural Testing (DAST) - A Status Report" *Journal of Aircraft*, Volume 16, Issue 8, 1979 https://doi.org/10.2514/3.58558

26. C. Hwang, E. Johnson and W. Pi, "Recent development of the YF-17 active flutter suppression system", 21st Structures, Structural Dynamics, and Materials Conference. 12 May 1980 - 14 May 1980, https://doi.org/10.2514/6.1980-769

27. G. Reich, M. Charissa Lin and E. Crawley, "An active aeroelastic wing model for vibration and flutter suppression", 36th Structures, Structural Dynamics and Materials Conference, 10 April 1995 - 13 April 1995, https://doi.org/10.2514/6.1995-1193

28. J.E. Cooper, R.G. Cook, G. Francois, O. de la Torre, S.A. Neild, M.H. Lowenberg, S.S. Alexander, E.B. Coetzee, M. Evans, Wind Tunnel Testing of a High Aspect Ratio Wing Model, International Forum on Aeroelasticity and Structural Dynamics IFASD 2019 9-13 June 2019, Savannah, Georgia, USA

29. "The LMS Test.Lab Manual", Rev 12A, LMS International 2012.

30. Di Leone, D., Lo Balbo, F., De Gaspari, A., and Ricci, S., "Model Updating and Aeroelastic Correlation of a Scaled Wind Tunnel Model for Active Flutter Suppression Test", *Aerospace* 2021, 8, 334, 1—24, 2021, doi: 10.3390/aerospace8110334

31. RTAI - the RealTime Application Interface for Linux, Department of Aerospace Science and Technology, Politecnico di Milano, 2021, https://www.rtai.org/?Homepage.

32. De Gaspari, A., Mannarino, A., and Mantegazza, P., "A dual loop strategy for the design of a control surface actuation system with nonlinear limitations", *Mechanical Systems and Signal Processing*, 90(2017):334–349, 2017, doi: 10.1016/j.ymssp.2016.12.037

33. De Gaspari, A. and Mantegazza, P., "Dual loop servo positioning using $PI^{(n+m)}$ controller", to be published in Mechanical Systems and Signal Processing.

34. NASTRAN, M. S. C., et al. Quick reference guide. MSC. SOFTWARE, 2004, 1.

35. Cavagna, L., Ricci, S. and Travaglini, L., "NeoCASS: an integrated tool for structural sizing, aeroelastic analysis and MDO at conceptual design level" *Progress in Aerospace Sciences*, vol. 47, no. 8, pp. 621–635, 2011.

36. Cavagna, L., Ricci, S. and Travaglini, L., "Structural sizing and aeroelastic optimization in aircraft conceptual design using NeoCASS suite," in 13th AIAA/ISSMO Multidisciplinary Analysis Optimization Conference, p. 9076, 2010.

37. Cavagna, L., Ricci, S. and Riccobene, L., "A fast tool for structural sizing, aeroelastic analysis and optimization in aircraft conceptual design," in 50th AIAA/ASME/ASCE/AHS/ASC Structures, Structural Dynamics, and Materials Conference 17th AIAA/ASME/AHS Adaptive Structures Conference 11th AIAA No, p. 2571, 2009.

38. Cavagna, L., Ricci, S. and Riccobene, L., "Structural sizing, aeroelastic analysis, and optimization in aircraft conceptual design," Journal of Aircraft, vol. 48, no. 6, pp. 1840–1855, 2011.

39. Ripepi, M. and Mantegazza, P., "Improved Matrix Fraction Approximation of Aerodynamic Transfer Matrices", *AIAA Journal*, Volume 51, Issue 5, https://doi.org/10.2514/1.J052009

40. Berg, J.K., Morgansen, K., Livne, E., Riccobene, L., Fonte, Toffol, F., De Gaspari, A., Marchetti, L., Ricci, S. and Mantegazza, P., "Analytical and Experimental Evaluation of Multivariable Stability Margins in Active Flutter

41. Syrmos, V., Abdallah, C., Dorato, P., and Grigoriadis, K., "Static output feedback—A survey," *Automatica*, Vol. 33, No. 2, 1997, pp. 125–137. https://doi.org/10.1016/S0005-1098(96)00141-0.

42. Ghiringhelli, G. L., Lanz, M., and Mantegazza, P., "Active flutter suppression for a wing model," *Journal of Aircraft*, Vol. 27, No. 4, 1990, pp. 334–341. https://doi.org/10.2514/3.25277.

43. Ghiringhelli, G. L., Lanz, M., Mantegazza, P., and Ricci, S., "Active Flutter Suppression Techniques in Aircraft Wings" *Control and Dynamic Systems*, Vol. 92, 1992, pp. 57–115. https://doi.org/10.1016/B978-0-12-012752-8.50007-6.

44. Fonte, F., Ricci, S., and Mantegazza, P., "Gust load allevfeedback" *Journal of Aircraft*, Vol. 52, No. 5, 2015, pp. 1559–1574. https://doi.org/10.2514/1.C032995.

45. Skogestad, S., and Postlethwaite, I., Multivariable feedback control: analysis and design, 2nd ed., Wiley-Interscience, 2005.

46. Nelles, O. Nonlinear System Identification: From Classical Approaches to Neuralnetworks and Fuzzy Models. Appl. Ther. 2001, 6, 717–721.

47. Peeters, B., et al., "The PolyMAX Frequency-Domain Method: A New Standard for Modal Parameter Estimation?": Hindawi Limited, 2004, *Shock and Vibration*, Vol. 11, p. 395–409.

48. G. Ghiringhelli, M. Lanz, P. Mantegazza: "A comparison of methods used for the identification of flutter from experimental data," *Journal of Sound and Vibration*, Nov. 1987, pp. 39-51.

49. Broussard, J. R., and Halyo, N., "Active flutter control using discrete optimal constrained dynamic compensators," 1983 American Control Conference, IEEE, 1983, pp. 1026–1034. https://doi.org/10.23919/ACC.1983.4788265.

50. Kwakernaak, H., and Sivan, R., Linear Optimal Control Systems, Wiley-interscience New York, 1972.

51. Losser, Y., "Ajustement de lois de commande application en aéronautique," Ph.D. Thesis, École nationale supérieure de l'aéronautique et de l'espace, Toulouse, 2006.

52. Patil, M. J., and Hodges, D. H., "Output Feedback Control of the Nonlinear Aeroelastic Response of a Slender Wing," *Journal of Guidance*, Control, and Dynamics, Vol. 25, No. 2, 2002, pp. 302–308. https://doi.org/10.2514/2.4882.

53. Miyazawa, Y., and Dowell, E., "Robust control system design with multiple model approach and its application to active flutter control," Guidance, Navigation and Control Conference, American Institute of Aeronautics and Astronautics, Reston, Virigina, 1989, pp. 1989–3578. https://doi.org/10.2514/6.1989-3578, AIAA Paper 1989-357.

54. Levine, W., and Athans, M., "On the determination of the optimal constant output feedback gains for linear multivariable systems," IEEE Transactions on Automatic Control, Vol. 15, No. 1, 1970, pp. 44–48. https://doi.org/10.1109/TAC.1970.1099363.

55. Moerder, D., and Calise, A., "Convergence of a numerical algorithm for calculating optimal output feedback gains," IEEE Transactions on Automatic Control, Vol. 30, No. 9, 1985, pp. 900–903. https://doi.org/10.1109/TAC.1985.1104073

56. Anderson, B. D., and Moore, J. B., Optimal Control, Linear Quadratic Methods, Prentice-Hall, 1990.

57. Bingulac, S., Cuk, N., and Calovic, M., "Calculation of optimum feedback gains for output-constrained regulators," IEEE Transactions on Automatic Control, Vol. 20, No. 1, 1975, pp. 164–166. https://doi.org/10.1109/TAC.1975.1100863.

58. Collins, E., Haddad, W., and Ying, S., "Reduced-order dynamic compensation using the Hyland-Bernstein optimal projection equations," Proceedings of 1995 American Control Conference - ACC'95, Vol. 1, American Autom Control Council, 1995, pp.539–543. https://doi.org/10.1109/ACC.1995.529307.

59. Dardel, M., and Bakhtiari-Nejad, F., "Limit cycle oscillation control of wing with static output feedback control method," *Aerospace Science and Technology*, Vol. 24, No. 1, 2013, pp. 147–160. https://doi.org/10.1016/j.ast.2011.08.013

60. Rautert, T., and Sachs, E. W., "Computational Design of Optimal Output Feedback Controllers," *SIAM Journal on Optimization*, Vol. 7, No. 3, 1997, pp. 837–852. https://doi.org/10.1137/S1052623495290441.

61. Toivonen, H. T., and Mäkilä, P. M., "Newton's method for solving parametric linear quadratic control problems," *International Journal of Control*, Vol. 46, No. 3, 1987, pp. 897–911. https://doi.org/10.1080/00207178708547402.

Appendix A: The SOF controller

Static Output Feedback controller can be seen as an extension of the quadratic optimal control case where only the system output is available for control instead of the full state vector. From one aspect this is an advantage since the output is already available without the need of an observer and this leads to a simpler controller structure. On the other hand, not having the full state vector means that there is the possibility of "missing" a part of the states and in turn performances can be significantly limited. This is also a direct consequence of minimizing the same cost function with the same weight matrices as in the optimal control, but with a lower number of available parameters, namely the elements of the output gain matrix $\boldsymbol{G}$ which are less in number than the elements of the state feedback matrix used in optimal control. For this reason, this type of control is said to be sub-optimal. However, its main disadvantage lies in the impossibility to obtain an analytic solution of the performance optimization problem in the form similar or equivalent to the Riccati equation of linear optimal control, and this results in having to handle a large numerical optimization problem in which it is necessary to minimize a complex expression depending implicitly on $\boldsymbol{G}$.

The great simplicity of SOF controllers makes them attractive in many applications where simple control laws are desired. For example, they are particularly well suited for massively controlled distributed systems, where actuator clusters are commanded only through a co-located set of sensors, i.e., only by groups of sensors located in the neighborhood of each actuator. To increase its overall performance, it would be easy to complement a SOF with a low-order dynamic regulator, designing the coupled static-dynamic controller through the same tools used for a purely static counterpart [49].

Owing to their simplicity, SOF regulators can also be used as backups, activated after a failure of a master system [50]. Another case in which SOF design techniques can be used is when some parameters of an existing controller must be re-tuned while preserving its structure [51]. Finally, it is far simpler to schedule and interpolate the elements of a SOF gain matrix than the parameters of a dynamic controller, making it suitable, by gain scheduling, for varying operating conditions.

An example of an aeronautical application of SOF controllers is provided by the work of [52], where a SOF controller was used for the flutter suppression and gust alleviation of a HALE aircraft. The work also showed that a proper choice of the sensor locations provided results similar to those achievable by the use of an ideal full- state linear quadratic regulator. In the work described in [53], SOF flutter suppression was used based on a multi-model approach,

i.e., weighting several different models within a single quadratic cost function, thus leading to a controller insensitive to the uncertainties structured within the accounted models. Another SOF active flutter suppression controller, using a direct digital design and including a size-constrained dynamic compensator, can be found in [49].

A common optimization approach in SOF is based on the solution of Lyapunov equations, having the closed-loop state matrix as coefficients. Within such a framework, many existing algorithms support a first-order gradient-based optimization, such as the legacy Levine–Athans algorithm [54], often revised as in [55], whereas a different approach can be found in work by Anderson and Moore [56].

Second-order optimization algorithms have also been proposed in [57], [58], [59], where the optimization is carried out on a state variance matrix instead of on a gain matrix, with the results being computationally very expensive when dealing with relatively large problems. The Anderson–Moore method [56] was modified to achieve superlinear convergence in [61] by introducing an approximation of the gain Hessian matrix. In [60] it was further enhanced with the computation of exact second derivatives of the cost function with respect to the gain matrix. Actually, its implementation was based on the iterative solution of a system of three coupled matrix equations, without any actual explicit calculation of the gain Hessian matrix. Another often-used solution method is the adoption of general-purpose state-of-the-art optimization functions, either unconstrained or constrained, for which the user has to provide the support to compute its own objective, gradient, and (possibly) Hessian.

The strategy adopted here to minimize the objective function applies a second order approximation to it, computing its Hessian matrix and then finding the stationary solution through a simple Levenberg–Marquardt modified Newton–Raphson iteration, as implemented in [47] The unknowns of the cost function are the elements of the gain matrix. The dimension of the gain matrix depends on the choice of the quantities acquired through the measurement. Though not used in the present work that focuses on control gains, the vector of optimization unknowns can also be extended to include any system parameter available for optimization.